



The influence of synthesis conditions on the visible-light triggered photocatalytic activity of g-C₃N₄/TiO₂ composites used in AOPs

Matevž Roškarič^a, Gregor Žerjav^{a,*}, Janez Zavašnik^b, Albin Pintar^a

^a Laboratory for Environmental Sciences and Engineering, Department of Inorganic Chemistry and Technology, National Institute of Chemistry, Hajdrihova 19, SI-1001 Ljubljana, Slovenia

^b Centre for Electron Microscopy and Microanalysis, Jožef Stefan Institute, Jamova 39, SI-1000 Ljubljana, Slovenia

ARTICLE INFO

Editor: Dr. G. Palmisano

Keywords:

TiO₂
g-C₃N₄
g-C₃N₄/TiO₂ composites
Heterogeneous photocatalysis
Bisphenol A
Visible-light illumination
Optimal weight concentration

ABSTRACT

Different synthesis temperatures (450–550 °C) were applied to synthesize g-C₃N₄ with the highest visible-light triggered photocatalytic activity. The best performing g-C₃N₄ photocatalyst was synthesized at 550 °C due to the created favourable structure that expressed the lowest band gap and charge carrier recombination rate. To further improve the photocatalytic activity of g-C₃N₄, different g-C₃N₄/TiO₂ (gCN/TNP) composites with varying weight concentrations of g-C₃N₄ and TiO₂ were prepared. Charge carrier separation was enabled due to the injection of photogenerated electrons from the g-C₃N₄ conduction band (CB) to the TiO₂ CB, where they reacted with water-dissolved oxygen to form reactive oxygen species. The best performing composite was 0.50gCN/TNP 2 h with 50 wt% of g-C₃N₄ and 2 h calcination at 350 °C. The improved photocatalytic activity is due to an appropriate ratio between the shielding effect of TiO₂, higher contact area and the consecutive improvement of the charge carrier separation, which is the key determining factor.

1. Introduction

With the increase of the world population and industrialization, the problem of wastewater treatment is increasing. Annually, more and more wastewater is generated, with negative economic and ecological consequences [1,2]. Due to modernization, wastewater streams contain pollutants that cannot be degraded using conventional biological treatment, so the use of advanced oxidation processes (AOPs) is reasonable. Among them, heterogeneous photocatalysis is proving to be a promising technology to purify wastewater and to convert solar energy into chemical energy [3,4]. In the process of heterogeneous photocatalysis, light is employed to trigger the catalytic activity of a semi-conducting photocatalyst. To generate charge carriers (holes (h^+) and electrons (e^-)), the energy of the light has to be the same or higher than the band gap energy of the semiconductor. The generated charge carriers are further used for the formation of reactive oxygen species (ROS) that are involved in the oxidative mineralization of water-dissolved organic pollutants [1]. Typical ROS are hydroxyl radicals (OH·) and superoxide anionic radicals (O₂^{·-}) [5]. In addition, ROS representatives include NO₂[·], SO₄^{·-}, ¹O₂, H₂O₂ and others. Among all, OH· has the strongest oxidation potential and is nonselective. On the other hand, O₂^{·-} has the longest lifetime of all ROS but is more selective and has a

reduced oxidation potential [6].

The most widely used photocatalyst is titanium dioxide (TiO₂), as it has unique optical properties, high photochemical stability, low cost and non-toxicity [3]. However, TiO₂ has two major drawbacks: (i) high rate of electron-hole pair recombination, and (ii) wide band gap value (3.0–3.4 eV) [3,7]. Therefore, it can utilize only the ultraviolet part of the solar irradiation, which limits its usage. To eliminate these drawbacks, several different methods can be used: combining different polymorphs of TiO₂, doping with metals or non-metals, using different morphologies of TiO₂ or combining TiO₂ with other suitable semiconductors [1,3,4,7–12].

A promising organic semiconductor is graphitic carbon nitride (g-C₃N₄), as it only contains earth-abundant elements like carbon and nitrogen, which makes it a green alternative to other semiconductors. In addition, g-C₃N₄ has a relatively high chemical and thermal stability and a moderate band gap value that is suitable for visible-light absorption [3]. Due to the synthesis of different possible g-C₃N₄ structures, this material is a hot spot [13] in various research fields, like hydrogen production [14,15], CO₂ reduction [16], photocatalytic degradation of pollutants [17–19], etc. Nevertheless, pure g-C₃N₄ also has some drawbacks like fast charge carrier recombination rate and low specific surface area [3,9,13,17].

* Corresponding author.

E-mail address: gregor.zerjav@ki.si (G. Žerjav).

<https://doi.org/10.1016/j.jece.2022.107656>

Received 21 February 2022; Received in revised form 28 March 2022; Accepted 1 April 2022

Available online 7 April 2022

2213-3437/© 2022 The Author(s). Published by Elsevier Ltd. This is an open access article under the CC BY-NC-ND license (<http://creativecommons.org/licenses/by-nc-nd/4.0/>).

To eliminate the drawbacks of both photocatalysts, formation of a heterostructure between $g\text{-C}_3\text{N}_4$ and TiO_2 is favourable [3,17]. The efficiency of the $g\text{-C}_3\text{N}_4/\text{TiO}_2$ composite photocatalysts to degrade water-dissolved pollutants is dependent on their structural and optical properties, which are further dependent on the used weight concentration of $g\text{-C}_3\text{N}_4$. Ma et al. [20] found that 15 wt% of $g\text{-C}_3\text{N}_4$ is an optimal concentration to improve the photocatalytic activity. The improvement was three times higher compared to the reference TiO_2 hollow microspheres under visible-light illumination for rhodamine B dye degradation. Hao et al. [17] synthesized a macro/mesoporous $g\text{-C}_3\text{N}_4/\text{TiO}_2$ heterojunction photocatalyst, which, at the optimal $g\text{-C}_3\text{N}_4$ loading, exhibited a 7.2 and 3.1 times higher reaction rate constant for the degradation of rhodamine B dye under visible light than pure TiO_2 or pure $g\text{-C}_3\text{N}_4$. Kočí et al. [21] found similar effects, as a 1:2 ratio between TiO_2 and $g\text{-C}_3\text{N}_4$ in the formed heterostructured photocatalyst improved the photocatalytic degradation of N_2O under UVA irradiation compared to the pure components.

Nevertheless, thorough studies starting with the synthesis of the optimal $g\text{-C}_3\text{N}_4$ and a wider range of $g\text{-C}_3\text{N}_4$ weight concentrations in $g\text{-C}_3\text{N}_4/\text{TiO}_2$ composites are still absent. Therefore, the aim of the present work was first to synthesize an optimal $g\text{-C}_3\text{N}_4$ by varying the synthesis temperature from 450 to 550 °C and to evaluate the structural, optical and photocatalytic properties of the obtained pure $g\text{-C}_3\text{N}_4$. After obtaining the $g\text{-C}_3\text{N}_4$ with the highest photocatalytic activity under visible-light illumination, the obtained $g\text{-C}_3\text{N}_4$ was further used to prepare heterostructured $g\text{-C}_3\text{N}_4/\text{TiO}_2$ composite photocatalysts. Composites with different weight concentrations between $g\text{-C}_3\text{N}_4$ and TiO_2 were prepared to determine the optimal concentration between the components and gain further insight in the field of $g\text{-C}_3\text{N}_4$ and TiO_2 based photocatalysts for wastewater treatment. Further, the mortar milling $g\text{-C}_3\text{N}_4/\text{TiO}_2$ synthesis procedure was upgraded by annealing the composites at 350 °C for 2 h in air to obtain a better junction between both components.

2. Experimental

2.1. Synthesis of the photocatalysts

All chemicals used for the synthesis were of analytical grade and used without further purification. In all cases, ultrapure water (18.2 M Ω cm) was used. Dicyandiamide (Sigma Aldrich) was used to synthesize $g\text{-C}_3\text{N}_4$ with the following facile calcination procedure: heating from room temperature with a ramp of 300 °C/h to end temperature (450, 500 or 550 °C), which was held back for 4 h. After the synthesis, the photocatalysts were left to cool to room temperature. The synthesized photocatalysts were denoted as 450gCN, 500gCN and 550gCN.

For the synthesis of $g\text{-C}_3\text{N}_4/\text{TiO}_2$ composite photocatalysts, commercially available TiO_2 nanoparticles DT-51 (CristalACTiV™), denoted as TNP, and 550gCN were used. The components were combined by milling them in an agate mortar for 1 min in different weight concentrations (25, 50 and 75 wt% of 550gCN) to obtain the following photocatalysts: 0.25gCN/TNP, 0.50gCN/TNP and 0.75gCN/TNP. Further, the obtained photocatalysts were annealed in a muffle furnace (Nabertherm, Germany) at 350 °C for 2 h with a heating ramp of 300 °C/h and denoted as 0.25gCN/TNP 2 h, 0.50gCN/TNP 2 h and 0.75gCN/TNP 2 h.

2.2. Surface and textural characterization of prepared photocatalysts

The ATR-FTIR measurements were performed using a Perkin-Elmer FTIR Frontier spectrometer equipped with a PIKE Technologies GladiATR Vision™ accessory with a diamond crystal. The ATR-FTIR spectra (average of 40 spectra) of prepared photocatalysts were measured between 4000 and 600 cm^{-1} with a resolution of 4 cm^{-1} .

Composition of the prepared materials was determined by the X-ray powder diffraction (XRD) analysis performed on a PANalytical PRO

MPD diffractometer with $\text{Cu K}\alpha 1$ radiation (1.54056 Å) in the scan range of 10–90° in 0.034° increments. The PDF of standards were obtained from the International Centre for Diffraction Data.

To determine the specific surface area, pore volume and average pore size of the materials, N_2 physisorption experiments were carried out using a Micromeritics TriStar II 3020 instrument equipped with the SmartPrep degasser. Degasification was carried out in a N_2 stream (Linde, purity 6.0) as follows: 60 min at 90 °C and 240 min at 180 °C. After cooling, the measurements were performed at –196 °C. The Brunauer, Emmett and Teller (BET) theory was employed to obtain the specific surface area of the photocatalysts, whereas on the other hand, the Barret, Joyner and Halenda (BJH) theory was used to obtain the pore size distribution. Skeletal density and total pore volume of the prepared photocatalysts were investigated by means of helium pycnometry using a Micromeritics AccuPyc II 1340 instrument. After the calibration, a 1.0 mL cell was used to perform the measurements (averaged 10 measurements per sample).

The morphological analysis of the prepared materials was performed with a field-emission scanning electron microscope (FE-SEM) Carl Zeiss model SUPRA 35 VP, which was operated at 1 kV. The powdered nano-sized samples for TEM analyses were dispersed in EtOH(abs) and sonicated, and then drop-casted onto Cu-supported amorphous lacey carbon grids. Samples were mounted in multiple specimens holder (Mod. 677, Gatan Inc.) and analyzed in the transmission electron microscope (TEM, JEM-2100, JEOL Inc.) operating at 200 kV. The micrographs were recorded by a slow-scan CCD camera (Orius SC1000, Gatan, Inc.). In TEM, the chemical composition of the samples was assessed by an energy-dispersive X-ray spectrometer (EDS, Mod. EX-24063JGT, JEOL Inc.). For each spectrum, a spot EDS spectrum with 60 s live time was recorded at the representative location with high α -tilt towards the detector to minimise Cu artefact signal from the support grid; still, in the experimental spectra, we can observe a minor Cu artefact peak. For the presentation of the EDS results, the 0–5 kV energy window is considered as it comprises all the energy peaks of elements considered.

2.3. Optical characterization of photocatalysts

A Perkin-Elmer Lambda 35 UV-Vis spectrophotometer equipped with an RSA-PE-19 M Praying Mantis powder holder was employed to obtain the UV-Vis diffuse reflectance (UV-Vis-DR) spectra of the synthesized materials. Spectralon® was used for the background corrections. All the spectra were recorded in the absorbance mode from 800 to 250 nm with a scan rate of 240 nm/min and a 2.0 nm slit width. The Kubelka-Munk theory was used for the estimation of band gap values.

Solid photoluminescence (PL) spectra were recorded using a Perkin-Elmer LS-55 fluorescence spectrometer equipped with a solid plunger plate and powder sample holder. The excitation wavelength for samples containing $g\text{-C}_3\text{N}_4$ was 320 nm with a scan rate of 200 nm/min (from 350 to 620 nm) and an emission slit of 2.6 nm. For the TiO_2 samples, the excitation wavelength was 300 nm with a scan rate of 150 nm/min (from 340 to 560 nm) and an emission slit set to 5.5 nm.

2.4. OH-radical generation tests

For determination of OH-radical production rates, a photoluminescence method with the probe molecule coumarin (Alfa Aesar) was used. 10 mg of a photocatalyst was suspended in 50 mL of the aqueous solution of coumarin (1.4 mM). The suspension was stirred at 400 rpm for 30 min in the dark to establish the adsorption/desorption equilibrium. After the dark period, the samples were illuminated with a Schott visible-light lamp (model KL 1600 LED) equipped with an UV cut-off filter at 410 nm. Samples were taken at different times in the 180 min reaction timespan and filtered using a 0.2 μm regenerated cellulose membrane filter. 300 μL of the filtered solution was dissolved in a 10 mL volumetric flask with ultrapure water. The measurements were performed using a Perkin-Elmer LS-55 fluorescence spectrometer with the

liquid sample holder and quartz cuvette (Hellma Analytics, Art. No. 101–10–40). The excitation wavelength was 338 nm with a scan rate of 200 nm/min (from 200 to 600 nm) and an emission slit set to 10.0 nm.

2.5. Test of photocatalytic performance

All photocatalytic experiments were carried out in a batch slurry reactor (Lenz Laborglas, model LF60, 250 mL) made of glass, using water-dissolved bisphenol A (BPA, Aldrich) as a model pollutant and a 150 W halogen lamp (Philips) equipped with an UV cut-off filter at 410 nm. The photocatalytic oxidation tests were performed at atmospheric pressure and 20 °C using a Julabo thermostat (model F25/ME). 250 mL of aqueous solution of BPA ($c_0 = 10.0$ mg/L) was mixed together with the selected photocatalysts to form a suspension ($c_{\text{cat}} = 125$ mg/L). The BPA/

photocatalyst suspension was stirred at 600 rpm and purged with air at a rate of 45 L/h. Before illumination, the suspension was kept in the dark for 30 min to establish the sorption process equilibrium of BPA onto the catalyst surface. Samples were taken at different times in the 120 min reaction timespan and filtered using a 0.2 μm regenerated cellulose membrane filter.

The BPA degradation as a function of time was measured by means of a Thermo Scientific high-pressure liquid chromatograph (HPLC, model Spectra) equipped with a 100 \times 4.6 mm BDS Hypersil C18 (2.4 μm) column operating in isocratic mode. The mobile phase was a mixture of methanol (Merck) and ultrapure water (70:30 vol ratio) with a flow rate of 0.5 mL/min. The column and the autosampler were thermostated at 30 and 25 °C, respectively. The detection of BPA was carried out with an UV detector at a fixed wavelength of 210 nm.

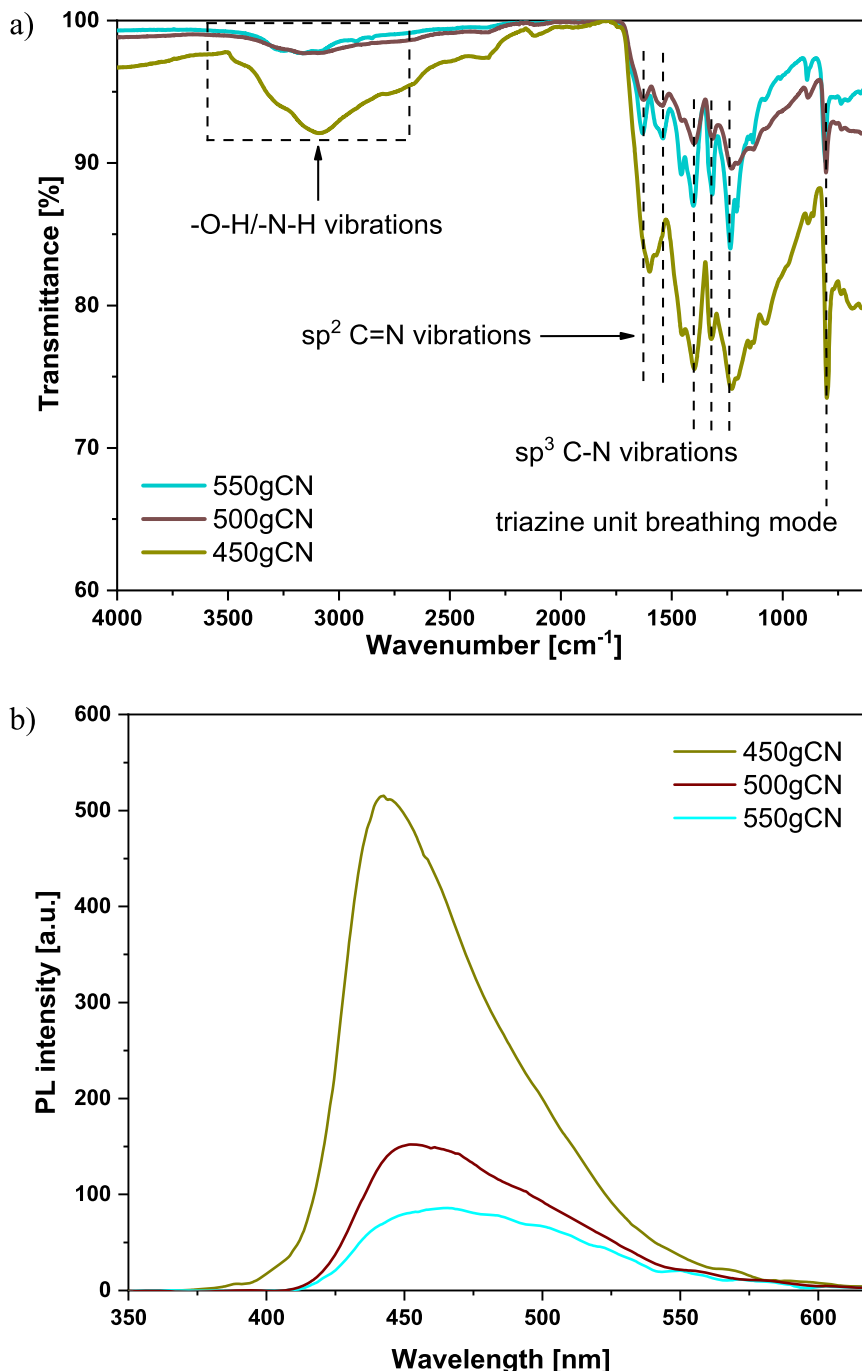


Fig. 1. a) ATR-FTIR spectra and b) solid photoluminescence spectra of selected pure g-C₃N₄ materials.

To determine the degree of mineralization at the end of BPA degradation experiments, total organic carbon (TOC) analysis was conducted on fresh and end-product solutions (after 120 min of visible-light illumination) using a Teledyne Tekmar Torch total organic carbon analyzer. The observed error of three repetitions was within $\pm 1\%$. By means of a Perkin-Elmer CHNS 2400 Series II analyzer, we determined the extent of carbon deposition on the catalyst surface after the photocatalytic oxidation reactions and calculated real mineralization (i.e. true TOC conversions). The elemental analysis of the weight content of carbon, hydrogen and nitrogen was also carried out using the same CHNS analyzer.

3. Results and discussion

3.1. Pure $g\text{-C}_3\text{N}_4$

To obtain pure $g\text{-C}_3\text{N}_4$ with the highest visible-light triggered photocatalytic activity for wastewater treatment, the temperature of the $g\text{-C}_3\text{N}_4$ synthesis varied between 450 and 550 °C, with a step of 50 °C. Further, the samples (450gCN, 500gCN and 550gCN) were analyzed to investigate their surface, structural and optical properties as well as their ability to generate ROS and degrade water-dissolved model organic pollutant bisphenol A (BPA).

3.1.1. Surface and textural analysis of pure $g\text{-C}_3\text{N}_4$ photocatalysts

To confirm a successful $g\text{-C}_3\text{N}_4$ synthesis, the ATR-FTIR measurements presented in Fig. 1a were performed. In all investigated samples, characteristic peaks in the range from 1700 to 1100 cm^{-1} for different C-N vibrations were observed, as well as the vibration mode for triazine ring unit at around 808 cm^{-1} [22]. Peaks at wavenumbers around 1389, 1317 and 1244 cm^{-1} can be attributed to the sp^3 C-N vibrations, and the peaks at around 1611 and 1534 cm^{-1} to the sp^2 C=N vibration [23]. In the range of 3500–3000 cm^{-1} , a broad peak was observed which corresponds either to surface adsorbed water or N-H terminal groups that were left from the polycondensation [22]. No other peaks were observed in the ATR-FTIR graphs, which provides a good indication of the high purity of the obtained $g\text{-C}_3\text{N}_4$ materials. The major difference in the shape and intensity of peaks between the investigated pure $g\text{-C}_3\text{N}_4$ samples can be noticed in the case of 450gCN sample. The origin of differences probably lies in the uncompleted polycondensation [24]; the 450gCN photocatalyst thus exhibits a larger peak in the range of 3500–3000 cm^{-1} . Minor differences in the ATR-FTIR spectra for the 500gCN and 550gCN samples can be attributed to the experimental uncertainty when the ATR mode is used [25,26].

The lower degree of polymerization for the 450gCN sample is also visible when comparing XRD patterns of derived materials presented in Fig. S1. For the 450gCN sample, the intensity of characteristic peaks at 13.2° (100) and 27.5° (002) (corresponding to PDF JCD 00–066–0813) is minimal and increases with the increase of synthesis temperature. The peak at around 13° corresponds to the plane of the tri-s-triazine unit of $g\text{-C}_3\text{N}_4$ with the inter-planar distance of 0.665 nm. The most intense peak at around 27° belongs to the inter-planar stacking of the plane for graphite-like materials with an inter-planar distance of 0.323 nm [19, 27]. The structure of $g\text{-C}_3\text{N}_4$ materials is formed during the polymerization, which orders the monomers. Therefore, a higher degree of order could represent a better degree of crystallinity and thus a completed/better polymerization of monomers. This is clearly seen in the case of 550gCN sample, which exhibits the most intense peaks among all three investigated pure $g\text{-C}_3\text{N}_4$ photocatalysts. This means that there is a larger concentration of molecules or crystals present with the same spacing (structure) [28]. Crystallite sizes were also calculated with the use of the Scherrer equation (Table S1). The listed results reveal that the crystallite size increases with the synthesis temperature, as was expected with a more complete polycondensation.

The results of N_2 physisorption and helium pycnometry analyses performed on pure $g\text{-C}_3\text{N}_4$ samples are presented in Table S1 and Fig. S2.

All three samples express a type IV isotherm with H3 hysteresis loops, which indicates a mesoporous structure with slit-like pores [20,29]. The analyzed photocatalysts exhibited low specific surface area, characteristic for $g\text{-C}_3\text{N}_4$ solids [9], although the specific surface area increased from 2.9 to 16.9 m^2/g with the increasing synthesis temperature (Table S1). Higher specific surface area of a photocatalyst usually beneficially influences the photocatalytic activity due to the improvement of its adsorption capability [17,30,31]. The pore size distribution was calculated applying the BJH theory; the obtained results show that the synthesis temperature did not influence the average pore diameter. On the other hand, the pore volume increased with increased synthesis temperature. This trend was also observed in the results of helium pycnometry measurements for the total pore volume, which also provided the data about the skeletal sample density that was increasing with the increased synthesis temperature. The obtained results provide another evidence that with the increase of synthesis temperature, a higher degree of polymerization is achieved and thus the wanted graphite-like structure is formed.

3.1.2. Optical properties

The optical properties of prepared pure $g\text{-C}_3\text{N}_4$ photocatalysts were examined by performing UV-Vis-DR and solid PL analyses. In the UV-Vis-DR spectra (Fig. S3), we can observe that all synthesized pure $g\text{-C}_3\text{N}_4$ samples exhibit the ability to absorb visible light. The band gap values were estimated using the Kubelka-Munk theory as presented in Eq. (1):

$$(\alpha hv)^2 = A(hv - E_g) \quad (1)$$

where α , hv , E_g and A are absorption coefficient, photon energy, direct band gap and proportional constant.

With the increase of the synthesis temperature, a red shift of the absorption edge was observed (Fig. S3), which has as the consequence that the band gap values become lower and therefore more of the visible-light spectrum can be utilized. The lowest band gap value was observed for the 550gCN photocatalyst, which agrees with the structural and textural analysis (see chapter 3.1.1). We would like to point out that the band gap values for 500gCN and 550gCN samples are nearly the same, but the specific surface area of the latter is about four times higher (Table S1), so we expect that the 550gCN sample would exhibit a higher photocatalytic activity than the 500gCN sample.

The solid photoluminescence (PL) measurements are a good tool to evaluate the recombination rate of charge carriers (electrons (e^-) and holes (h^+)). A higher intensity in the PL spectra means a faster charge carrier recombination rate, as PL (i.e. light emission) is generated during this process [32]. Thus, a higher PL means a decrease in the probability of the photocatalyst to generate reactive oxygen species (ROS; for example, hydroxyl radicals ($\text{OH}\cdot$) or superoxide anionic radicals ($\text{O}_2^{\cdot-}$)), which are responsible for the decomposition/mineralization of water-dissolved organic pollutants. Fig. 1b presents the results of solid PL measurements for pure $g\text{-C}_3\text{N}_4$ photocatalysts. For all samples, we observed a blue luminescence signal with a PL maximum at around 450 nm, which is characteristic for $g\text{-C}_3\text{N}_4$ materials [33]. A decrease in the PL intensity was observed with the increase of the synthesis temperature, which means that the lifetime of charge carriers is prolonged. This is probably due to the higher degree of polymerization with increasing synthesis temperature and the creation of the graphite-like structure. The improvement of the polymerization process also introduces some defects, which could act as shallow charge carrier traps and prolong their lifetime [33]. Nevertheless, the charge carrier recombination is still high, which is a well-known characteristic of $g\text{-C}_3\text{N}_4$ materials [9].

3.1.3. Hydroxyl radical generation and bisphenol A degradation tests

To gain further insight into the photocatalytic properties of prepared pure $g\text{-C}_3\text{N}_4$ samples, reactive oxygen species scavenger experiments

using water-dissolved coumarin as a probe molecule were performed to measure the OH·-generation rate via the formation of 7-hydroxycoumarin (7-HOCU). An absolute determination of 7-HOCU, and therefore OH·-radicals, is not possible due to the formation of other by-products, but the relative evaluation of a series of photocatalysts can be performed [34]. The temporal concentrations of 7-HOCU calculated from the calibration curve illustrated in Fig. S4 are presented in Fig. S5 over a 180 min interval of visible-light illumination. No generation of OH·-radicals was observed in the 30 min dark period, therefore the starting time is presented as 0 min. All pure g-C₃N₄ photocatalysts exhibited a visible-light response as was suggested in the UV-Vis-DR measurements (Fig. S3). The 550gCN sample was the most photocatalytically active toward the generation of OH·-radicals, tightly followed by the 500gCN solid. Furthermore, the prepared photocatalysts were tested for the degradation of water-dissolved bisphenol A under visible-light illumination (Fig. 2). The experimental set-up was kept in the dark for 30 min before illumination to establish the adsorption equilibrium of BPA onto the surface of the photocatalysts. We observed that only a negligible amount ($\leq 1\%$) of BPA was adsorbed on the surface of pure g-C₃N₄ materials. The most active photocatalyst for the BPA degradation after 120 min of visible-light illumination was the 550gCN sample with 11.4% of BPA degradation. This is probably due to its low band gap value, prolonged lifetime of charge carriers and the highest specific surface area among all prepared pure g-C₃N₄ materials.

Although the 550gCN sample exhibits the highest BPA degradation and OH·-radical generation rate among all three synthesized pure g-C₃N₄ photocatalysts, the photocatalytic activity is still low due to the overall low specific surface area and high recombination rate [9]. To eliminate the presented drawbacks of pure g-C₃N₄, we further used another semiconductor (titanium dioxide (TNP)) to prepare g-C₃N₄/TiO₂ composites with the aim to increase specific surface area and lower the charge carrier recombination rate.

3.2. g-C₃N₄/TiO₂ composite photocatalysts

Milling in an agate mortar was used to prepare the 550gCN/TNP composites with different weight concentrations between 550gCN and TNP (25, 50 and 75 wt% of 550gCN). Furthermore, the 550gCN/TNP

composites prepared in the agate mortar were annealed at 350 °C for 2 h in air. From the elemental analysis of the weight content of carbon and nitrogen (Table 1), we can observe that the nominal and actual values (considering the experimental error) of the weight content of g-C₃N₄ are nearly the same. In the case of the 0.25gCN/TNP photocatalyst, we observe 23.8 (mortar) and 21.2 (2 h calcination) wt% of carbon and nitrogen (combined), which is quite near the nominal value of 25 wt%. The same applies for the 0.50gCN/TNP and 0.75gCN/TNP series, which exhibit 46.6 (mortar), 45.4 (2 h calcination), 75.4 (mortar) and 74.1 (2 h calcination) wt%, respectively. The calcination procedure slightly decreases the carbon and nitrogen amount in the composites due to slight decomposition of g-C₃N₄.

3.2.1. Surface and textural analysis of g-C₃N₄/TiO₂ photocatalysts

The results of ATR-FTIR measurements performed on the prepared g-

Table 1

Results of N₂ physisorption (specific surface area, total pore volume and average pore diameter), CHNS elemental analysis (carbon and nitrogen in fresh samples), estimated band gap values from UV-Vis-DR measurements using Kubelka-Munk theory, and calculated crystallite size from the XRD patterns using the Scherrer equation for TNP @ 48°.

Sample	S _{BET} m ² / g	V _{pore} cm ³ / g	d _{pore} nm	C _{fresh} %	N _{fresh} %	Band gap eV	Crystallite size @ 48° nm
550gCN	16.9	0.08	20.4	34.1	61.2	2.72	–
TNP	85.8	0.29	13.7	1.4	–	3.28	22.4
0.25gCN/ TNP	72.2	0.25	14.0	8.7	15.1	3.20	22.3
0.25gCN/ TNP 2 h	71.7	0.26	13.3	8.1	13.1	3.19	22.2
0.50gCN/ TNP	57.0	0.22	15.9	17.7	28.9	3.09	22.4
0.50gCN/ TNP 2 h	49.5	0.21	16.8	17.6	27.8	3.12	22.4
0.75gCN/ TNP	31.9	0.12	15.9	26.6	48.8	2.68	22.1
0.75gCN/ TNP 2 h	29.5	0.12	16.4	25.9	48.2	2.71	22.0

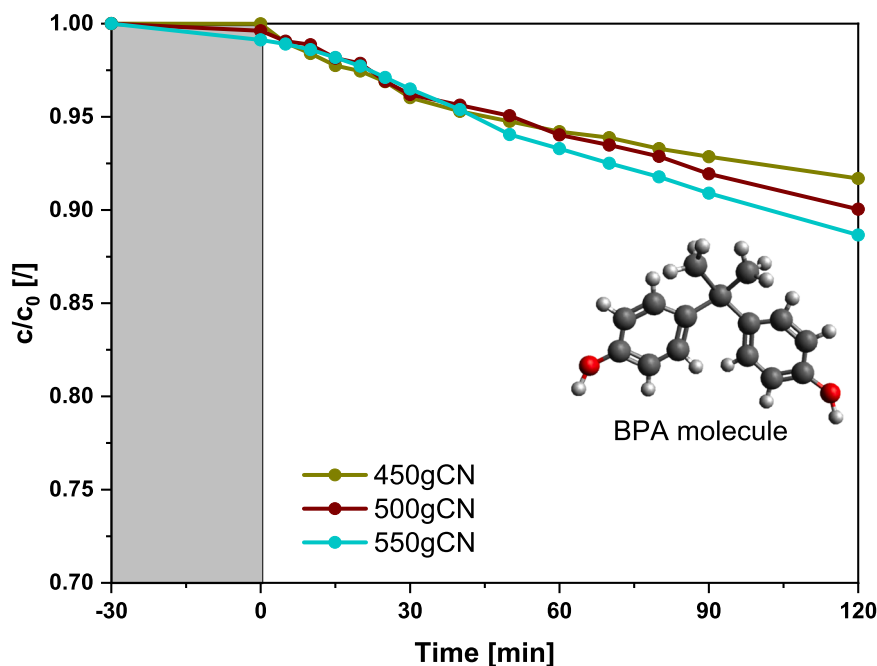


Fig. 2. Photocatalytic degradation of BPA ($c_0 = 10.0$ mg/L) conducted at $T = 25$ °C in the presence of selected g-C₃N₄ photocatalysts (125 mg/L) under visible-light illumination.

C_3N_4/TiO_2 composites are illustrated in Fig. 3. From these results, we can confirm that the characteristic peaks for 550gCN (see chapter 3.1.1) are all present in the composite photocatalysts. Furthermore, we can also observe a broad peak for the pure TNP, which is located between 800 and 400 cm^{-1} [35]. This peak is attributed to the stretching of Ti-O-Ti and Ti-O bonds [17] and is also present in the composite photocatalysts. Comparing the ATR-FTIR spectra of the composites with the

ATR-FTIR spectra of pure 550gCN sample, no shifts or changes in the shape of the characteristic peaks were observed, regardless of the utilized weight concentration and synthesis method. This means that both components are present in the composites without any major changes in their chemical structure, regardless of the used synthesis procedures. With the increase of the weight concentration of 550gCN in the composites from 25% to 50%, the absorbance increases and becomes stable when the amount of added 550gCN is increased further to 75%. These results suggest that the composites using a weight concentration of either 50 or 75% of 550gCN could behave similarly in the photocatalytic experiments.

The XRD patterns of the prepared composite materials are presented in Fig. 4. In the XRD pattern of pure TNP sample, we can observe characteristic peaks for anatase TiO_2 (corresponding to PDF JICDD 00-021-1272) with the two most intense peaks at around 25.3° (101) and 48.0° (200), and others at 37.8° (004), 53.9° (105), 55.1° (211) and 62.7° (204), respectively [17,21]. In the XRD patterns of the composites, the only peak for 550gCN is present at around 27.5° (002), but on the other hand, all the characteristic peaks for TNP are observed. This is probably due to the higher crystallinity and order of TNP in comparison to 550gCN and due to some overlapping of the peaks of both components [17]. No shifts of peaks in the XRD patterns of the composites in comparison to the peak positions in the XRD patterns of pure components were observed. This means that the structure of the components is not affected by the synthesis procedure and that TNP is probably located mostly on the surface of 550gCN, instead of being incorporated into the lattice of 550gCN [17,21]. Using the Scherrer equation for the spherical particles, we estimated the crystallite size of TNP for the peak at 48.0° due to the overlapping of the most intense TiO_2 peak at 25.3° , with the peak of 550gCN at 27.5° . The values listed in Table 1 show that the crystallite size of TiO_2 is constant for all investigated samples.

The results of N_2 physisorption analysis of the prepared composites are presented in Fig. 5 and Table 1. The obtained N_2 adsorption/desorption isotherms (Fig. 5a) show that all investigated materials exhibit type IV isotherms with H3 hysteresis loops, which indicates a mesoporous structure with slit-like pores [4,20,29]. Further, we observed that the pure TNP sample ($85.8\text{ m}^2/\text{g}$) has five times higher specific surface area than the pure 550gCN sample ($16.9\text{ m}^2/\text{g}$), and that with the increasing weight content of 550gCN in the composites, their specific surface area decreases. The calcination process slightly decreases the specific surface area of the composites, regardless of the used weight concentration. The explanation for this phenomenon might be in the thermal stability of g- C_3N_4 , which can be problematic at higher temperatures. The results show that the calcination at 350°C is sufficient to slightly decompose and change the 550gCN structure in the g- C_3N_4/TiO_2 composites, and that with increasing of the weight content of 550gCN in the composites, this phenomenon becomes even more expressed. This slight degradation could be beneficial as it could lead to a higher contact area and consequently to a stronger interaction between the components. Furthermore, we can conclude from Fig. 5b that the TNP pores dominate the pore size distribution in the composite photocatalysts. With decreasing of the weight amount of 550gCN, the pore volume increases and is nearly the same as for pure TNP. On the other hand, the trend for the pore diameter is opposite, but the changes are minor when different weight concentrations of 550gCN are used. Regardless of this trend, the calcination process at a selected weight concentration does not change the pore volume and average pore diameter significantly.

For better illustration of the effects caused by different weight ratios between the components (as indicated from the results of other characterizations (Figs. 3–5)), we performed SEM analysis of the prepared materials. SEM micrographs of pure 550gCN photocatalyst are presented in Fig. 6a. We can observe large irregular structures in plate forms like pebbles. Further, it can be observed that the structures are porous, as was suggested by the results of N_2 physisorption analysis (Fig. S2). For the pure TNP sample (Fig. 6b), we can observe aggregates of small TiO_2

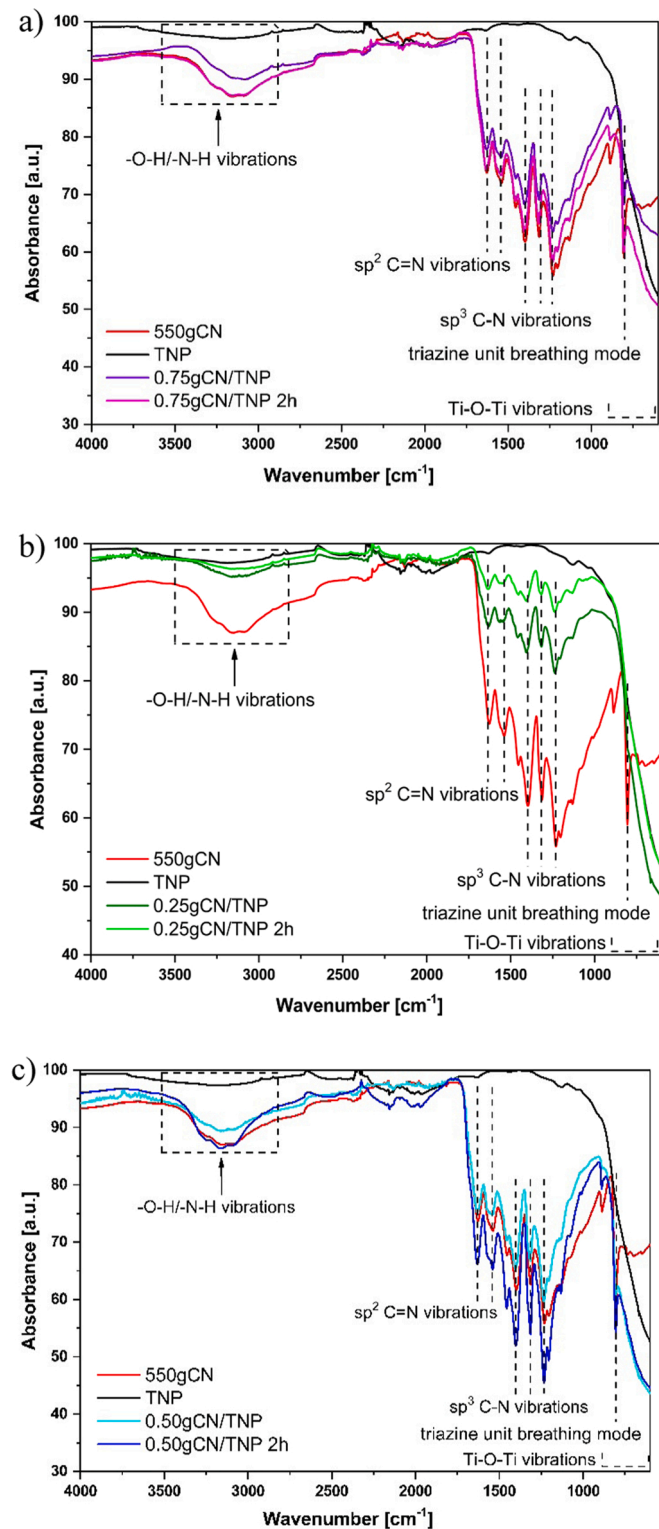


Fig. 3. ATR-FTIR spectra of composite samples containing different weight concentrations of 550gCN: a) 75%, b) 50%, and c) 25%.

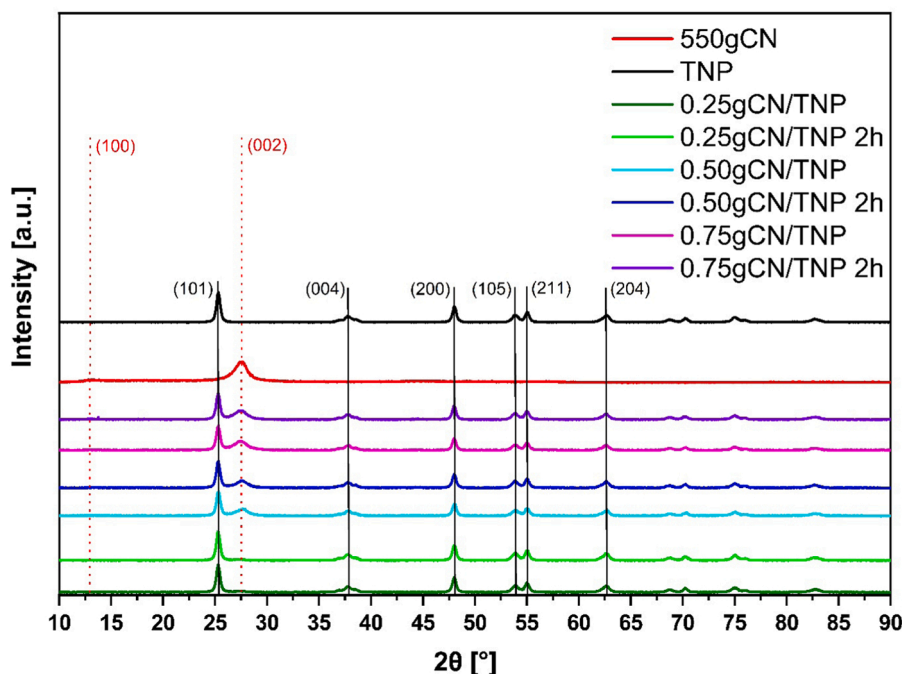


Fig. 4. XRD patterns of selected photocatalysts. The dotted red vertical lines correspond to the pure $g\text{-C}_3\text{N}_4$ standard peaks (corresponding to PDF JCDD 00-066-0813) and the full black vertical lines to the TiO_2 standard peaks (corresponding to PDF JCDD 00-021-1272).

spherical nanoparticles. The structure again appears to be porous as was suggested above by N_2 physisorption examination (Fig. 5). In Fig. 7, SEM micrographs of the composites prepared with both synthesis procedures are presented. No major changes of TNP or 550gCN structures were observed in all the composites compared to the structure of pure components. As seen in these SEM images, TNP is deposited onto the surface of 550gCN aggregates, which is in good agreement with the results of XRD analysis (Fig. 4) and is reported in the literature [13,21,36]. For the same content of 550gCN, no major differences are observed when the mortar composite is annealed for 2 h as was expected from the results of other analyses already discussed before (Figs. 3–5). However, major changes are observed with the increasing amount of added $g\text{-C}_3\text{N}_4$ in the composites. In case of 0.25gCN/TNP composites, it is clearly seen that the major component is TNP and that 550gCN is consequently nearly completely covered with TNP. With increasing of the 550gCN amount to 75%, the surface coverage with TNP decreases. This could have an impact on the catalytic activity of the composites under visible-light illumination; as more of the 550gCN surface is covered with TNP, less visible light can be utilized due to the shielding effect, in this case caused by TNP [20,36]. On the other hand, TNP has a larger specific surface area that could be beneficial, as TNP is used in the composites to separate charge carriers, generated by 550gCN under visible-light illumination. Therefore, a suitable coverage of the 550gCN surface with TNP is needed to have a sufficient contact area between both components in order to successfully separate charge carriers [17,21].

We additionally performed TEM analysis to obtain a more in-depth structural and textural analysis, results of which are summarized in Fig. 8. For the pure TNP sample, the observed nanoparticles are crystalline, with an average size of the crystallites of up to 10 nm (Fig. 8a). The chemical composition by standard-less energy-dispersive X-ray spectroscopy (EDS) showed the presence of only Ti and O; as calculated by the thin-film approximation method, the Ti:O ratio is approx. 32:68. The phase composition, as identified by the selected-area electron diffraction pattern (SAED), confirms that the sample consists of single-phase TiO_2 -anatase, which concurs with the XRD analysis. Further, the 550gCN sample in the TEM appears as thin, plate-like wrinkled, thin sheets (Fig. 8b). At higher magnifications, the sample appears

amorphous, without any long-range ordering. The SAED consists of weak diffuse rings, which are similar to a simulated SAED graphite pattern. The spot EDS analysis showed the presence of C and N in about 50:50 ratio.

On the TEM micrographs for the composite photocatalysts (0.25gCN/TNP 2 h, 0.50gCN/TNP 2 h and 0.75gCN/TNP 2 h), we can distinguish the crystalline TNP nanoparticles from 550gCN by their stronger diffraction contrast (Fig. 8c, d and e). The TNP-anatase nanoparticles are concentrated on the edges of 550gCN sheets and intertwined in the wrinkles but can also be scattered throughout the 550gCN support. The relative concentration of both phases is hard to estimate from the micrographs alone, but overall, the number of observed TNP crystallites increases consistently with the nominal loading. The chemical composition was assessed by spot EDS analysis on representative mixtures and confirmed the combination of all expected elements: C, N, O and Ti in different ratios. The quantitative chemical composition calculations from EDS spectra are strongly affected by local nano-scale inhomogeneities, such as agglomerations of several TNPs and non-uniform thickness of the 550gCN and TNP, and therefore highly inaccurate. Still, from the EDS peak intensity ratio, we can conclude on the increasing TNP trend corresponding to nominal loading.

To obtain further insights onto the effect of the optimal weight amount of $g\text{-C}_3\text{N}_4$, optical properties of the materials were determined.

3.2.2. Optical properties

By means of UV-Vis-DR measurements, we determined light absorption properties of the composite catalysts as well as estimated band gap values using the Kubelka-Munk theory (Eq. (1)). From the UV-Vis-DR results, we also estimated the edge potentials of the valence band (E_{VB}) and conduction band (E_{CB}) of TNP and 550gCN solids using Eqs. (2) and (3):

$$E_{VB} = \chi - E^c + \frac{1}{2}E_g \quad (2)$$

$$E_{CB} = E_{VB} - E_g \quad (3)$$

where E_g is the band gap value of 550gCN (2.72 eV) and TNP (3.28 eV),

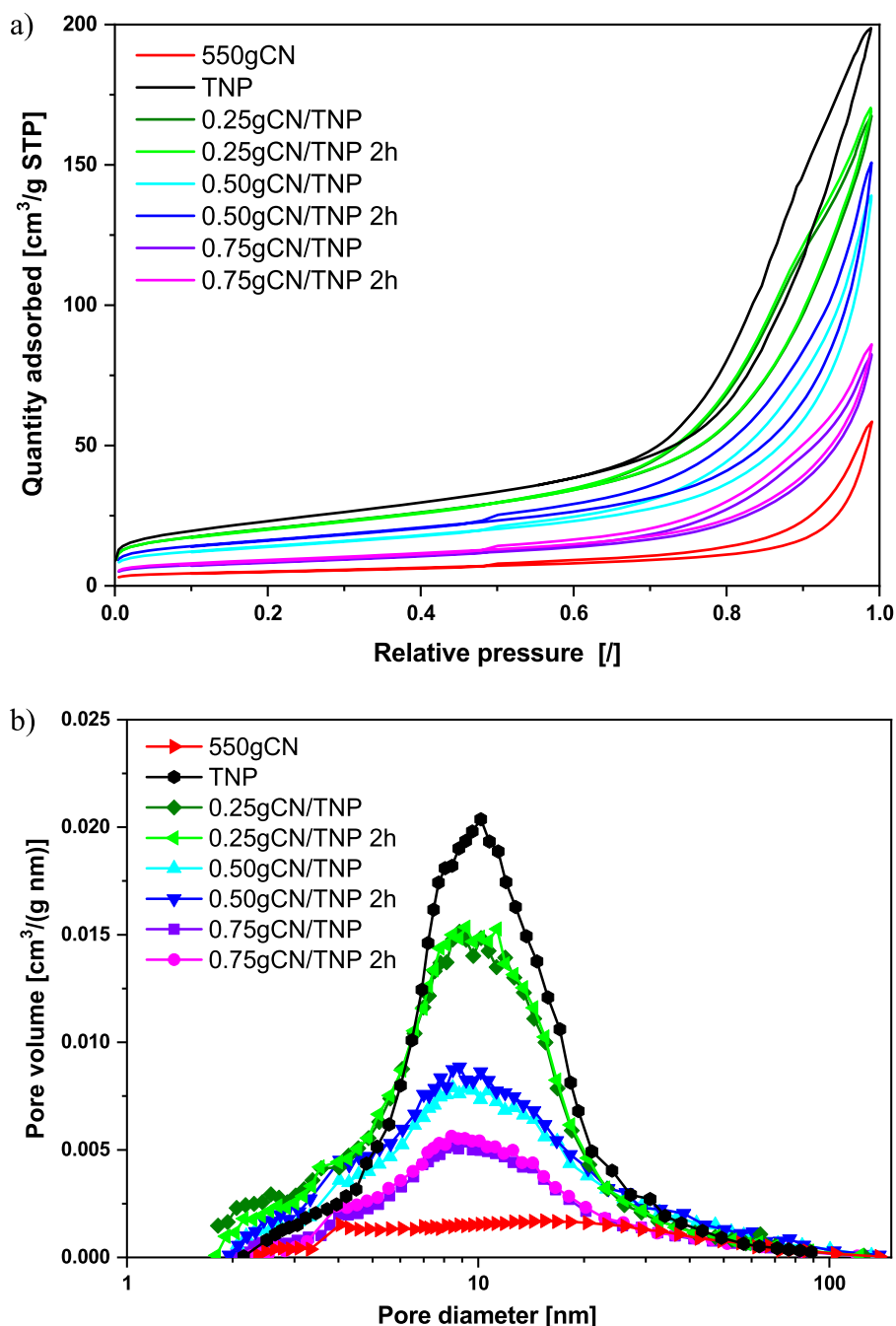


Fig. 5. Results of N₂ physisorption analysis for selected photocatalysts: a) adsorption/desorption isotherms, and b) pore size distribution.

χ is the electronegativity, which is the geometric mean of the constituent atoms and has a value of 4.73 eV for 550gCN and 5.81 eV for TNP, and E^e the energy of free electrons on the hydrogen scale (4.5 eV vs. NHE) [17]. Using Eqs. (2) and (3), the estimated edge potentials for the valence band are 1.59 and 2.95 eV for 550gCN and TNP, and the estimated edge potentials for the conduction band of 550gCN and TNP are -1.13 and -0.33 eV, respectively.

These properties are crucial for the evaluation of photocatalysts, since the light absorption properties define the efficiency of a photocatalyst using visible-light illumination. From Fig. 9a, we can observe that the pure TNP sample exhibits only UV-light absorption (band gap of 3.28 eV) in contrast to the pure 550gCN sample (band gap of 2.72 eV), which also has broader visible-light absorption. The lower band gap value in the 550gCN solid is present due to the charge transfer response from the N 2p orbital valence band to the C 2p orbital conduction band

[17]. As the structure of the components in all examined composites did not change significantly (see chapter 3.2.1), it is of no surprise that the composites are able to absorb both visible and UV light. Consequently, the band gap values of the composites are in between the values of pure TNP and pure 550gCN solids. When comparing different synthesis procedures while keeping the weight concentration constant, we can again observe that there are no significant changes. Due to a higher amount of TNP (75%) in the case of 0.25gCN/TNP composites, the band gap value was found to be higher (the absorption edge is blue shifted) compared to the band gap values of other composite photocatalysts, and quite nearly the same as the one of the pure TNP sample. The same behaviour can be observed for the 0.75gCN/TNP composites, but in the other direction, as in terms of the band gap value (absorption edge is red shifted), they behave nearly the same as the pure 550gCN sample. As expected, the 0.50gCN/TNP composites behave within the range defined by other

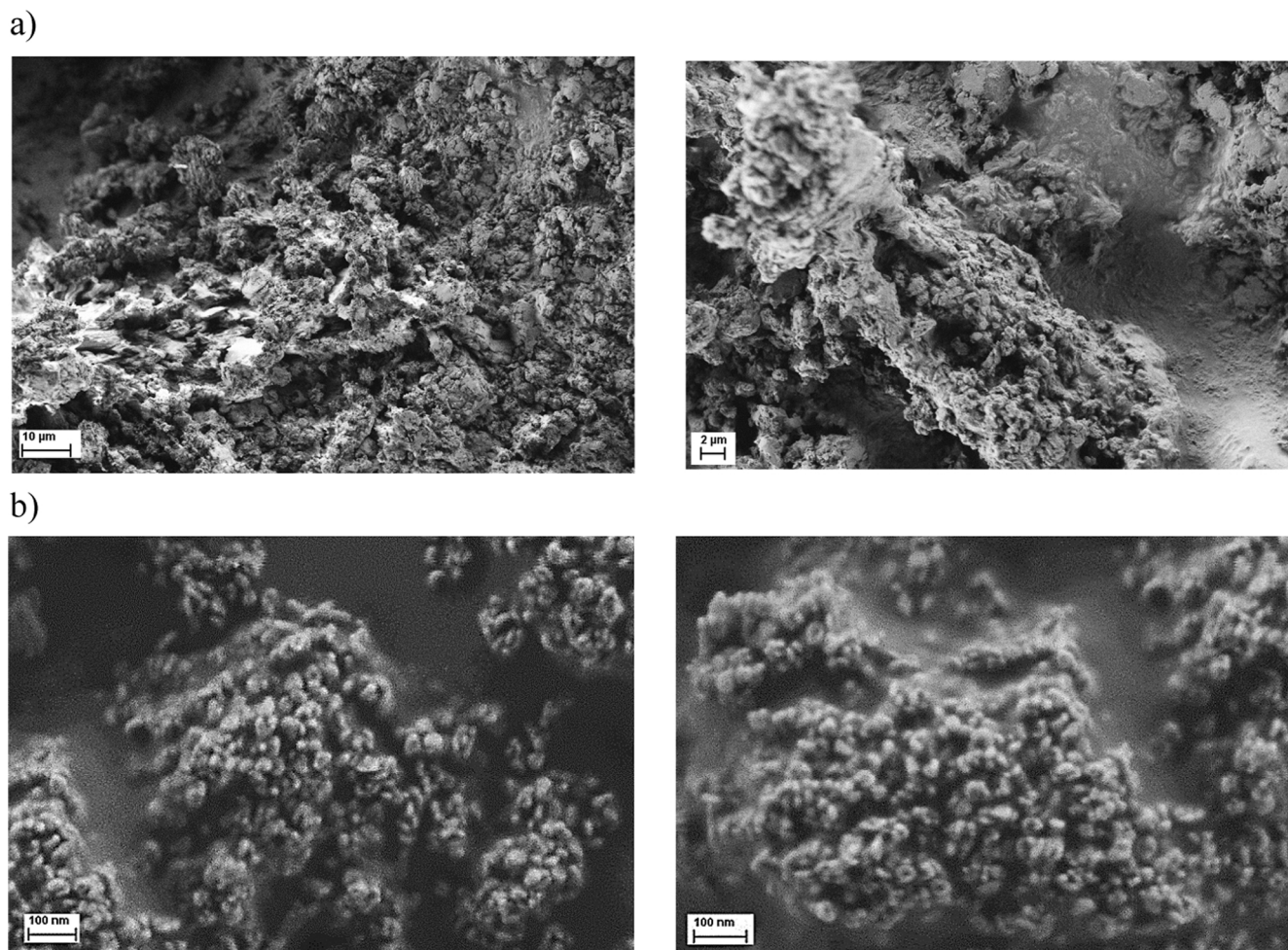


Fig. 6. SEM images of pure 550gCN (a) and pure TNP (b) samples obtained at different magnifications.

composites. In general, a lower band gap value means that a wider range of the visible-light spectrum can be utilized and thus the photocatalytic activity can increase. On the other hand, a lower band gap value also increases the tendency for the charge carrier recombination [37].

To investigate the recombination of charge carriers, we performed the solid PL measurements on the investigated composites [4]. All the PL measurements illustrated in Fig. 9b were performed using parameters optimal for 550gCN, since TNP requires a different excitation wavelength. Therefore, the curve for the pure TNP photocatalyst in Fig. 9b is flat, which could be falsely interpreted as a low charge carrier recombination rate, since it is known that pure TiO₂ in anatase polymorph (TNP) has quite high charge carrier recombination rate [38]. For illustration, Fig. S6 shows the PL spectra of pure TNP acquired at appropriate settings. From Figs. S6 and 9b, we can conclude that in the composites 550gCN dominates the PL spectra, because they exhibit a blue luminescence signal with a PL maximum at around 450 nm. The signal originates due to the presence of the following states in g-C₃N₄ materials: sp³ C-N σ band, sp² C-N π band and the lone pair (LP) state of the bridge nitride atom. Therefore, we can observe three transitions in the combined PL spectra (Fig. 9b) of the selected photocatalysts: σ* -LP, π* -LP and π* -π [33]. These transitions are the origin of the high charge carrier recombination rate for the pure 550gCN photocatalyst [9]. Therefore, it makes sense to combine g-C₃N₄ materials with the TiO₂ semiconductor and through charge carrier separation decrease the rate of charge carrier recombination. This is seen in Fig. 9b, where we successfully decreased the charge carrier recombination rate regardless of the used weight content of 550gCN. When the mortar composites are annealed, some improvement in the charge carrier separation is

observed as the PL maximum intensity decreases (Fig. 9b). This is probably due to the increased contact area between the components (see N₂ physisorption measurements in chapter 3.2.1) and increased strength of interaction, which in turn enabled better charge carrier separation. Nevertheless, the decrease of the PL maximum in all cases lies in the fact that the conduction band (CB) potential levels between TNP and 550gCN are appropriate (Fig. 9a and Eqs. (2) and (3)) and thus separate the charge carriers through the injection of visible-light generated electrons from CB of 550gCN to CB of TNP [17,35,39]. The injection of photogenerated electrons into the CB of TNP decreases the chances of π* -LP and π* -π relaxation emissions in 550gCN and is possible due to the created heterostructure as seen in the SEM and TEM analysis (Figs 7 and 8), where TNP clusters are deposited onto the surface of 550gCN aggregates [17,21].

A deconvolution of the solid PL spectra for the pure 550gCN sample and photocatalysts annealed for 2 h was performed using a Gaussian fit model as seen in Fig. 10 and Table S2. Four different Gaussian peaks were needed to fit the PL spectra adequately. It was already discussed in chapter 3.2.1 that the 0.25gCN/TNP composite photocatalysts behave nearly like pure TNP, which is the reason for the “false” low PL signal in Fig. 9b, as a different excitation wavelength is required to excite TNP. Therefore, the deconvoluted peaks 1–3 probably correspond to the transitions of pure TNP as seen in Fig. S6, although some red shift was observed compared to the values reported in the literature [8], the origin of which lies in some weak interactions between 550gCN and TNP even at low weight concentrations like 25% (see chapter 3.2.1 for XRD analysis and Fig. 4). Further, peak 4 at around 476 nm probably corresponds to the PL emission of 550gCN. For the other three analyzed

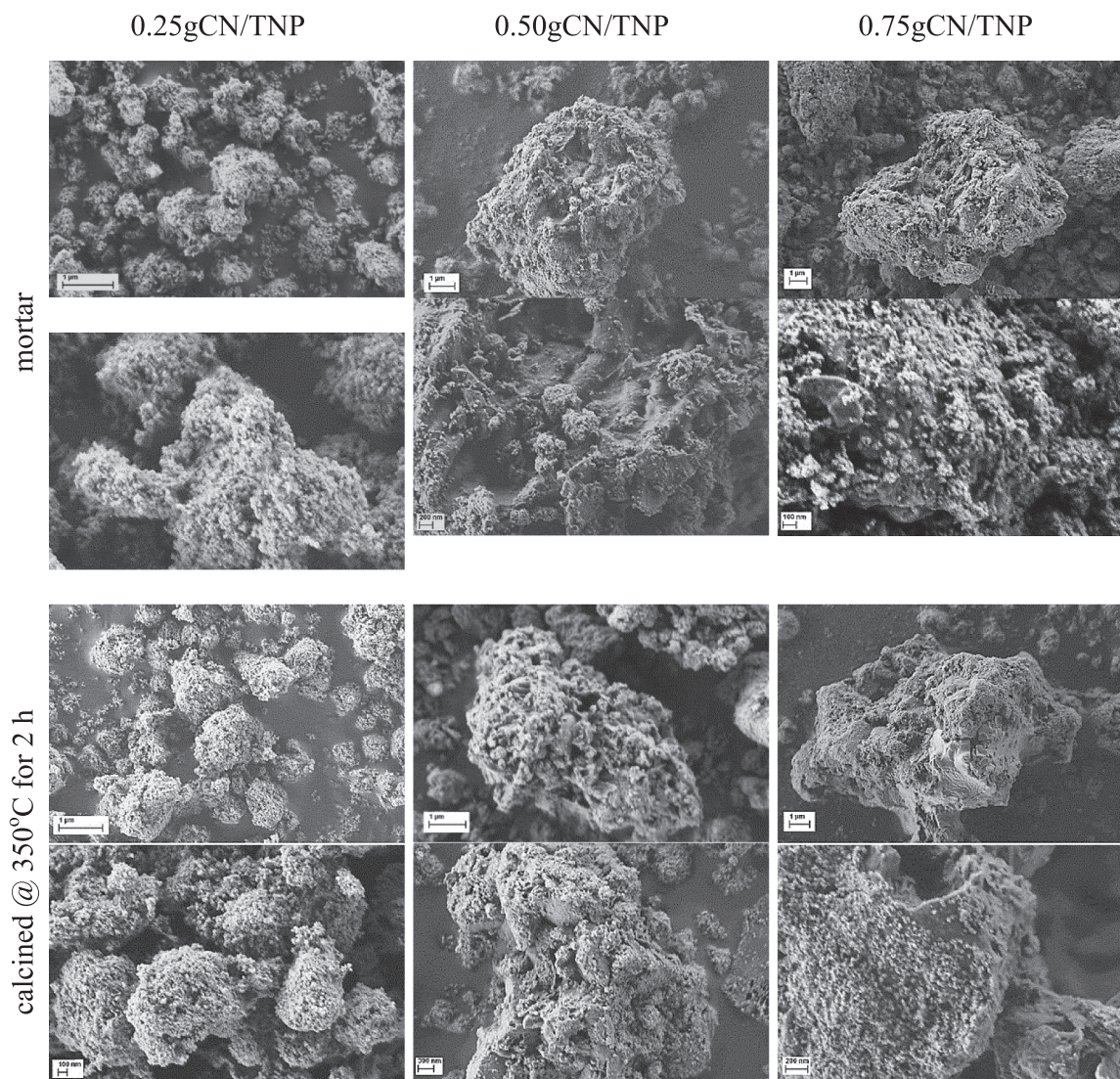


Fig. 7. SEM images of $g\text{-C}_3\text{N}_4/\text{TiO}_2$ composite photocatalysts obtained at different magnifications.

photocatalysts, peak 1 at around 438 nm (2.83 eV) corresponds to the $\sigma^* \text{-LP}$ emission, peak 2 at around 453 nm (2.74 eV) corresponds to the $\pi^* \text{-LP}$ emission and peak 3 at around 485 nm (2.56 eV) corresponds to the $\pi^* \text{-}\pi$ emission [33]. Peak 4 at around 530 nm (2.34 eV) can either correspond to the $\pi^* \text{-}\pi$ emissions [40] or can be a shallow trap of TNP [8]. Except for the 0.25gCN/TNP composites, no shifts in the positions of peaks 1–3 were observed within the experimental uncertainty, regardless of the used 550gCN weight content. The same is observed for peak 4 when pure 550gCN or 0.50gCN/TNP composites are used. There is, however, a blue shift in the position of peak 4 when 75 wt% of 550gCN is used. The composite 0.75gCN/TNP 2 h behaves similarly to the pure 550gCN sample and has therefore the lowest specific surface area among all the composite photocatalysts (Table 1). This could mean that in this solid most of the TNP is deposited on the surface and only a small amount of TNP is deposited in the pores of 550gCN. The majority of TNP present on the surface could have an influence on the PL measurements, and thus the blue shift appeared. Due to the higher amount of 550gCN, it is also expected that more $\pi^* \text{-}\pi$ emissions appear. Some shifts in the PL spectra could therefore occur from the dipole interaction between π^* and π electron states in 550gCN and TNP [21]. We also observed that the PL intensity of peaks 2 and 3 decreased, when the $g\text{-C}_3\text{N}_4$ weight content decreased from 100% to 50%, which means that the $\pi^* \text{-LP}$ and $\pi^* \text{-}\pi$ emissions occur less intensively because of the aforementioned

injection of photogenerated electrons from 550gCN CB to the TNP CB (Eqs. (2) and (3)). To achieve the most intense injection of the photo-generated electrons, an optimal amount of $g\text{-C}_3\text{N}_4$ is needed [17,21]. The 0.50gCN/TNP composites contain in our case the optimal amount of 550gCN, as they exhibit the highest charge carrier separation (i.e. the lowest overall PL emission maximum) compared to pure 550gCN sample and 0.75gCN/TNP composites, which increases the chance for the formation of ROS.

3.2.3. Hydroxyl radical generation test

In heterogeneous photocatalytic reactions, OH-radicals can be formed directly where photogenerated holes react with surface adsorbed water or -OH functional groups, or indirectly, where first the superoxide anionic radical ($\text{O}_2^{\cdot-}$) is formed utilizing photogenerated electrons and water-dissolved oxygen. The $\text{O}_2^{\cdot-}$ can form H_2O_2 , which then decomposes to form OH-radicals [34,41]. The indirect pathway is usually typical for $g\text{-C}_3\text{N}_4$ photocatalysts, and the direct one is typical for TiO_2 [6].

In Fig. 11, we observe no generation of OH-radicals in the 30 min long dark period, therefore the starting time is presented as 0 min. From the measurements for bare TNP and 550gCN samples, we also calculated the theoretical results that would occur in the presence of mortar composites when no beneficial interactions would be present. From the

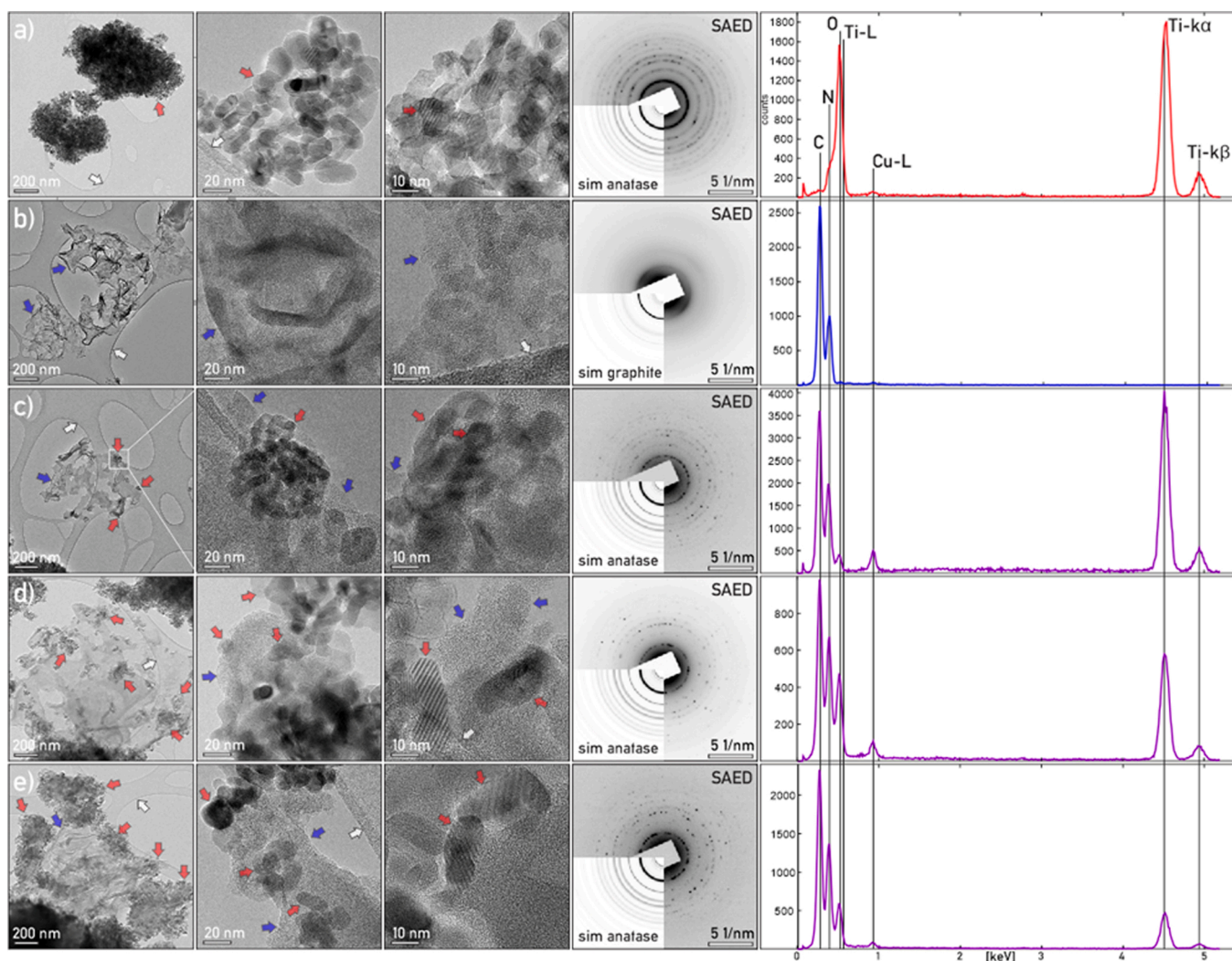


Fig. 8. Set of TEM micrographs recorded at the same magnifications of pure (a) TNP - titania nanoparticles and (b) pure 550gCN sample (g-C₃N₄), followed by mixtures of both phases: (c) 0.25gCN/TNP 2 h, (d) 0.50gCN/TNP 2 h, and (e) 0.75gCN/TNP 2 h. To guide the eye, the white arrows mark the edge of the amorphous lacy carbon support, the red arrows mark the TNP, and blue arrows mark the 550gCN. The micrographs are supplemented by SAED with a corresponding ab-initio simulation in the third quadrant inset; the crystalline TNP phase corresponds to TiO₂ - anatase, while electron diffraction from amorphous-like 550gCN sample results in broad diffuse rings similar to graphite. EDS spot spectra were recorded at the representative spots; note the overlapping of C, N, O and Ti in the first 0.3–0.6 keV.

results displayed in Fig. 11, we observe that under visible-light illumination, all tested photocatalysts exhibited generation of OH·-radicals, even the pure TNP, although only to a very minor extent. The visible-light activity of pure TNP sample can be explained with the presence of surface defects as a result of the manufacturer's synthesis procedure. However, from the obtained results (Fig. 11) we can conclude that all mortar composites exhibit a higher OH·-generation rate than expected based on simple theoretical calculations. The origin lies in the injection of photogenerated electrons from 550gCN CB to TNP CB, thus reducing the charge carrier recombination rate, as seen also in lower solid PL maximum values (Fig. 9b). After the annealing process, the photocatalytic activity of derived materials increases, which could be because of better interface contact created between the components, as was expected from the results of solid PL (Fig. 9b) and N₂ physisorption measurements (Fig. 5).

For an easier comparison of the influence of 550gCN weight content on the generation rate of 7-HOCU, all the coumarin results were combined in a bar graph presented in Fig. 11d. When the content of 550gCN increased from 25% to 50%, the generation of OH·-radicals increased. However, when the content of 550gCN increased further to 75%, a decrease of the formation of OH·-radicals was observed. The values of the

specific surface area for the 0.50gCN/TNP composites are in the mid-range of the investigated composites, and therefore specific surface area is not the key factor determining the photocatalytic activity of the composites. No significant differences are also present in the XRD patterns of 0.50gCN/TNP and 0.75gCN/TNP composites (Fig. 4), which is also true for the obtained ATR-FTIR spectra (Fig. 3). Therefore, we can thus exclude the structural differences as the determining factor for improving the photocatalytic activity. However, the parabolic trend in the photocatalytic activity can be explained using the results of SEM, TEM, PL and UV-Vis-DR analyses (Figs. 7–10). For the 0.25gCN/TNP composites, we can observe a high coverage of the 550gCN surface with TNP. This coverage acts as a shield layer that enables only a limited flux of visible light to reach the surface of 550gCN and trigger its photocatalytic activity [20]. On the other hand, in the case of 0.75gCN/TNP composites, the surface of 550gCN component is less covered with TNP, therefore the total interface area between the components is decreased, which limits the efficiency for the charge carrier separation (Fig. 9b). The origin of the highest OH·-radical formation rate of 0.50gCN/TNP composites lies therefore in the optimal coverage that enables the 550gCN to absorb enough visible light to generate charge carriers and at the same time to improve their separation [17,21,42].

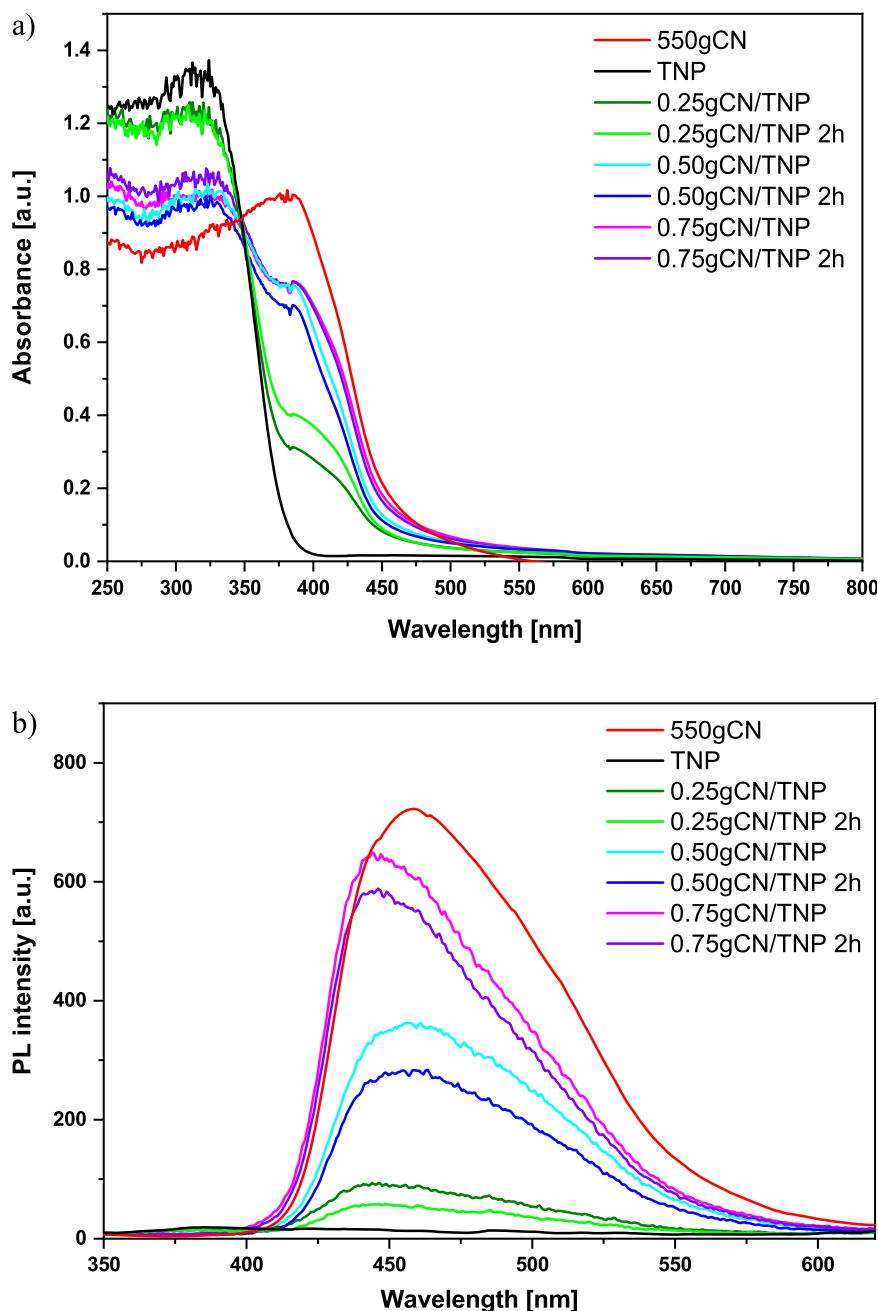


Fig. 9. Results of a) UV-Vis-DR measurements, and b) solid PL experiments for selected photocatalysts.

3.2.4. Test of photocatalytic performance

The photocatalytic activity of the synthesized composites was further evaluated by performing degradation tests under visible-light illumination using bisphenol A (BPA) as a model organic pollutant. From the BPA degradation results obtained in the presence of pure components, predictions were made also to investigate whether some beneficial interactions onto the photocatalytic activity would appear for the mortar composites. The results of the BPA degradation tests in Fig. 12a show that the pure TNP degraded only a slight amount of BPA under visible-light illumination due to its large band gap value (3.28 eV). Pure 550gCN showed some photocatalytic response, but the low specific surface area and fast charge carrier recombination rate limited its ability to considerably degrade BPA. We can also observe that the predicted values for the mortar composites are lower than the obtained experimental values. This shows again that this synthesis approach enables good enough surface coverage of TNP and strong enough interactions

between the components, thus enabling the prolongation of the “lifetime” of charge carriers (Fig. 9b). If the mortar composites are annealed at 350 °C, the photocatalytic activity toward BPA degradation improves, which is in agreement with the results of OH-generation tests presented in chapter 3.2.3.

As the 2 h annealing synthesis approach produces a larger interface area between the components, thus hindering the charge carrier recombination, we decided to demonstrate this by performing a kinetic analysis. Assuming that the photocatalytic liquid-phase oxidation of aqueous BPA solution undergoes a pseudo-first order kinetics, we used Eq. (4) to calculate corresponding photodegradation reaction rate constants for various photocatalysts:

$$\ln\left(\frac{c_0}{c_t}\right) = kt \quad (4)$$

where c_0 is the initial BPA concentration, c_t the actual BPA

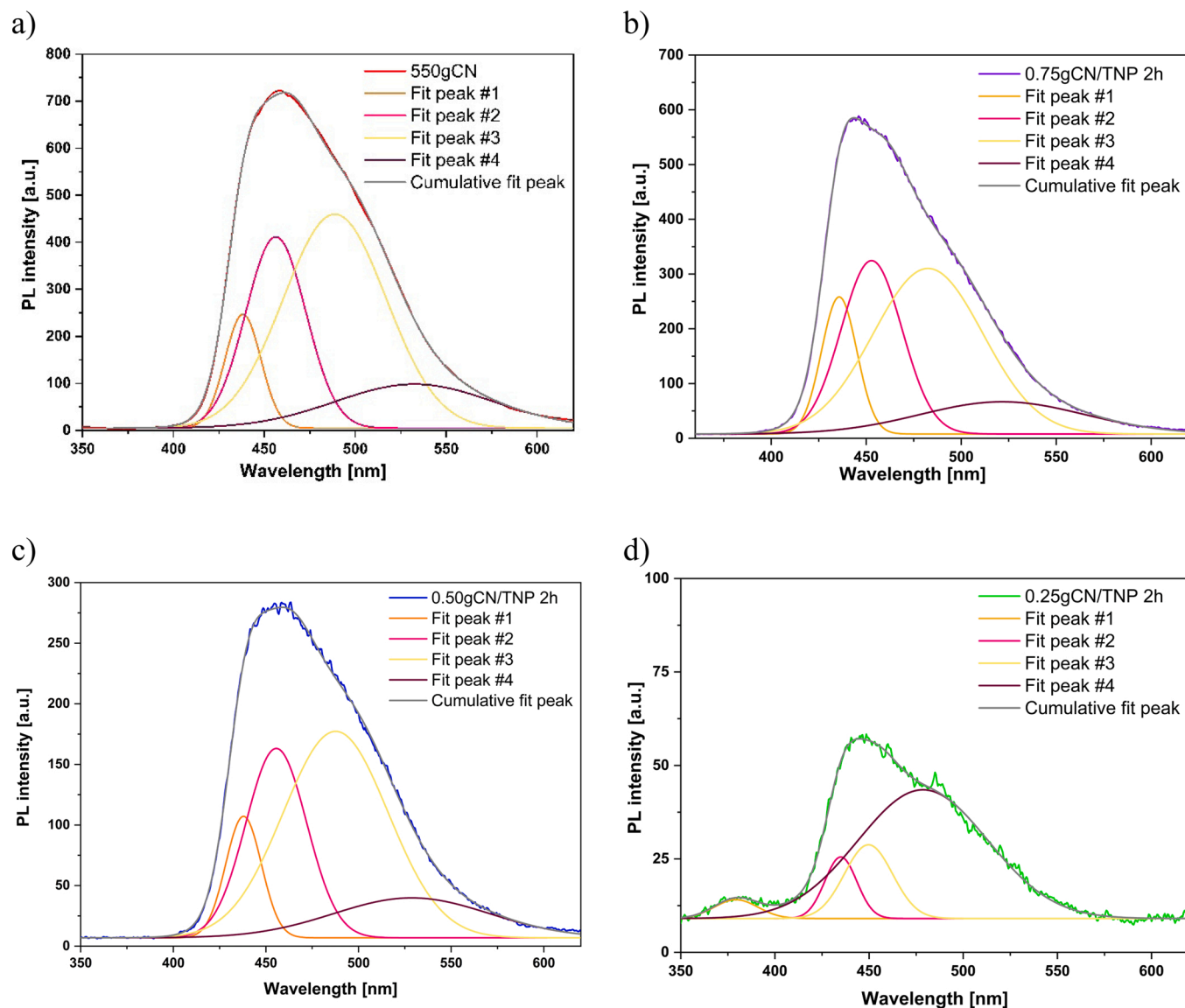


Fig. 10. Deconvoluted photoluminescence spectra for a) pure 550gCN, b) 0.75gCN/TNP 2 h, c) 0.50gCN/TNP 2 h, and d) 0.25gCN/TNP 2 h photocatalysts. Note that all the PL measurements were performed using parameters optimal for 550gCN, since TNP requires a different excitation wavelength. Therefore, the curve belonging to the pure 0.25gCN/TNP 2 h photocatalyst which contains high amount of TNP, could be falsely interpreted as a result of low charge carrier recombination.

concentration at a selected time, k the photodegradation reaction rate constant and t the selected time [43]. It can be seen in Fig. S7a that the linear fit of the proposed kinetic model fits the experimental data very well. From the results in Table 2 and Fig. S7a, it can be observed that the photodegradation rate among all investigated composites is the highest for 0.50gCN/TNP 2 h sample, which is 3.9 times higher than for the pure 550gCN solid and 16.4 times higher than for the pure TNP sample. This is in agreement with the results of optical analysis (chapter 3.2.2) and coumarin scavenger tests (chapter 3.2.3).

Finally, the results of TOC measurements for the annealed composites are presented in Fig. 12b and Table 2. Using the elemental analysis, we determined the extent of carbon deposition on the catalyst surface after the reaction, from which we calculated TOC accumulation and true TOC conversion, which corrects the measured one for the carbon deposition onto the surface of the photocatalyst. The results of TOC measurements follow the same trend as the results of BPA degradation runs and show only minor TOC accumulation occurrence for all the tested composites. We also performed the stability test by examining the most active photocatalyst 0.50gCN/TNP 2 h (Fig. S7b). It can be

observed that the photocatalytic activity decreases only slightly in five consecutive cycles using the same catalyst batch. Therefore, we can conclude that the best performing photocatalyst is a good candidate for the potential usage in the process of waste-water remediation.

3.2.5. Charge carrier excitation and migration mechanism

From literature [17,20,44] and the results of UV-Vis-DR (Fig. 9a) and solid PL (Figs. 9b and 10) measurements, we propose the photocatalytic charge carrier generation and separation mechanism shown in Fig. 13. Upon visible-light illumination, electrons are generated in the CB of 550gCN. Meanwhile the photogenerated holes remain in the 550gCN VB. In the pure 550gCN sample, these charge carriers are quickly recombined, thus limiting its photocatalytic efficiency (Fig. 9b). Pure TNP has a band gap value of 3.28 eV that is too high to generate charge carriers using visible-light illumination (Fig. 9a). In the g-C₃N₄/TiO₂ composites, the visible-light generated electrons can migrate from the 550gCN CB to the TNP CB due the fact that the CB edge potential of TNP (-0.33 eV vs. NHE) is less negative than the CB edge potential of 550gCN (-1.13 eV vs. NHE). This migration is possible because of the

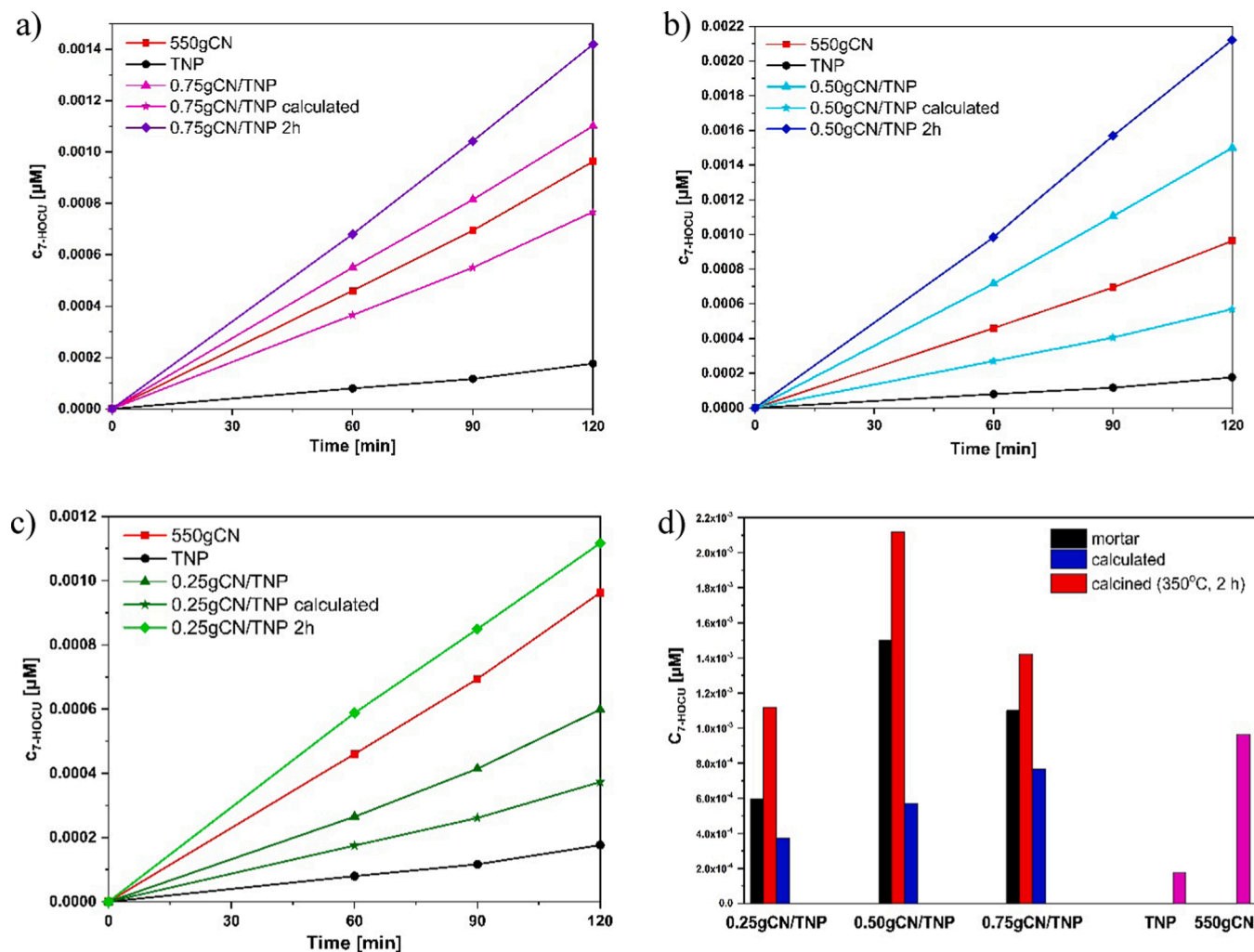


Fig. 11. Concentration of 7-HOCU under visible-light illumination for selected photocatalysts with different weight concentrations of 550gCN: a) 75%, b) 50%, c) 25%, and d) bar graph comparing all weight concentrations together.

formed heterostructure, which was described before (see chapters 3.2.1 and 3.2.2), and is a result of the powerful driving force that generates between the CB of both components, if the difference in its values is adequate [45,46]. The migrated electrons then react with water-dissolved oxygen and generate $O_2^{\cdot-}$, as the CB potential of both TNP and 550gCN are more negative than the reduction potential of oxygen (-0.046 eV vs. NHE) [47]. The generated $O_2^{\cdot-}$ can either attack water-dissolved BPA directly or form OH-radicals. The generated holes remain in the 550gCN VB, thus enabling a charge carrier separation as it was seen in the solid PL measurements (Fig. 9b) [17]. The potential for the OH \cdot /H $_2$ O (2.68 eV vs. NHE) and OH \cdot /OH $^-$ (1.99 vs. NHE) [48] is too positive for the holes in VB of 550gCN (1.59 eV vs. NHE) to produce OH-radicals. Therefore, the photogenerated holes probably directly attack the water-dissolved (and adsorbed) BPA, rather than generate OH-radicals.

The proposed type II heterojunction mechanism is in our case the most plausible, as only g-C $_3$ N $_4$ forms charge carriers under visible-light illumination. Therefore, no repellent Coulombic forces are present, as they would be if both semiconductors would produce charge carriers, and consequently a repel between photogenerated electrons/electrons and holes/holes would occur, which would then make the S-scheme mechanism plausible [49].

4. Conclusions

In conclusion, we have successfully synthesized three different g-C $_3$ N $_4$ materials using dicyandiamide as a precursor. The optimal synthesis temperature for g-C $_3$ N $_4$ was 550 °C, as it provided the most defined structure due to the successful polycondensation. Therefore, the 550gCN photocatalyst exhibited the highest specific surface area, lowest charge carrier recombination rate and favourable band gap value among all prepared pure g-C $_3$ N $_4$ photocatalysts, as well as the best photodegradation rate of bisphenol A (BPA) under visible-light illumination. To increase the photocatalytic activity of 550gCN, heterostructured composites with TiO $_2$ (TNP) were prepared by milling both components in a mortar. Further, the influence of the weight ratios between the components was investigated by changing the amount of 550gCN from 25 to 75 wt%. The mortar synthesis procedure of the composites was further upgraded by annealing the prepared composites at 350 °C for 2 h in air atmosphere. We determined the optimal weight content of 550gCN to be 50%, as the 0.50gCN/TNP 2 h composite exhibited the highest photocatalytic degradation and mineralization of BPA. The origin of the high photocatalytic activity of 0.50gCN/TNP 2 h composite lies in its still high specific surface area, narrow band gap and the lowest charge carrier recombination rate. Successful charge carrier separation, which is the key determining factor, was enabled due to the optimal distribution of TNP onto the surface of 550gCN (50 wt% content) and sufficiently high interface area that allowed the photogenerated

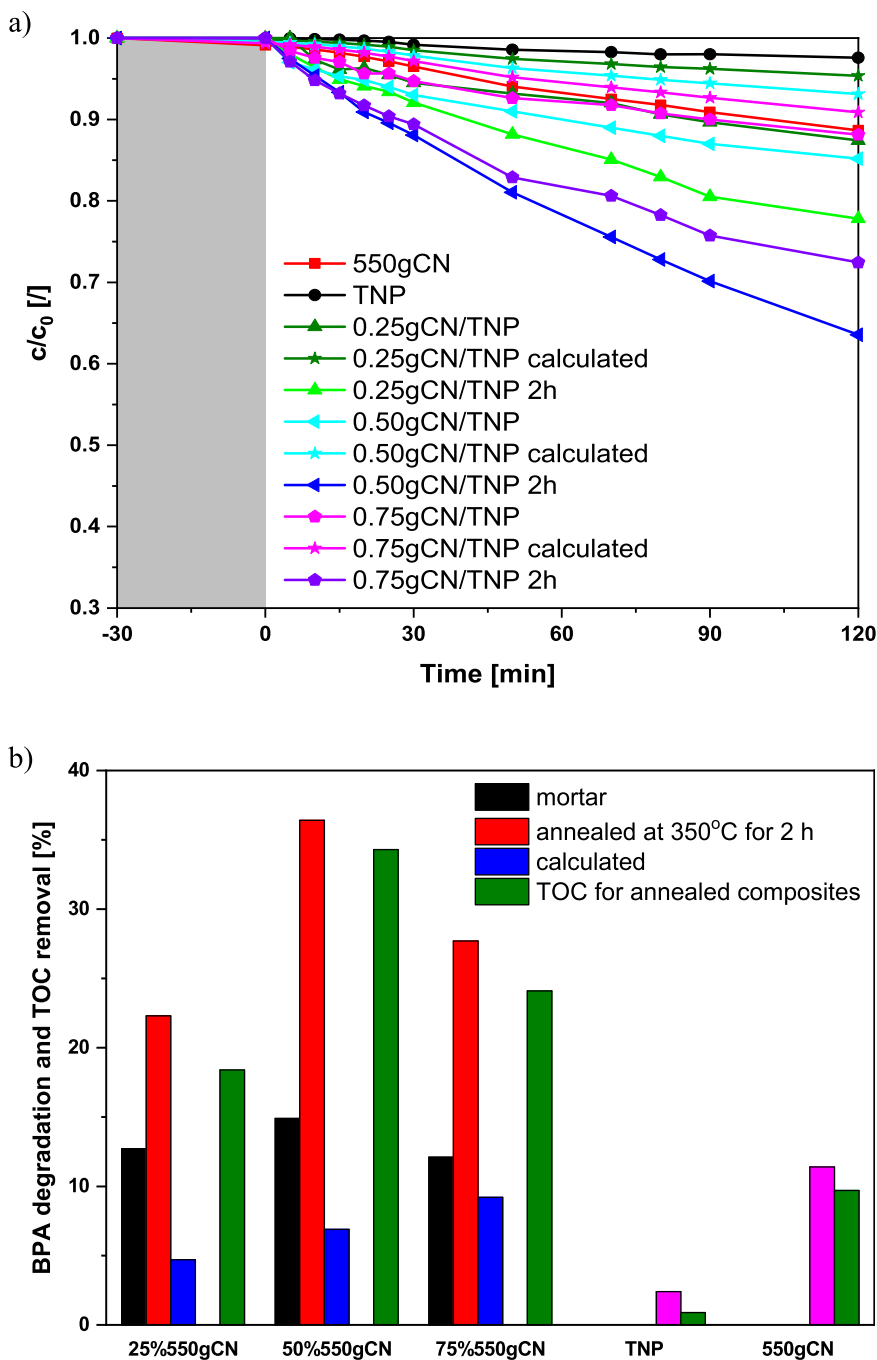


Fig. 12. Photocatalytic degradation of BPA ($c_0 = 10.0 \text{ mg/L}$) conducted at $T = 25 \text{ }^\circ\text{C}$ in the presence of selected photocatalysts (125 mg/L) under visible-light illumination: a) BPA degradation curves, and b) bar graph with TOC conversions for composites annealed for 2 h.

Table 2

Photodegradation reaction rate constants, differences in carbon content between fresh and used samples, and results of TOC measurements for pure samples and catalysts annealed for 2 h.

Sample	Photodegradation reaction rate constant min^{-1}	Difference in carbon %	TOC removal		
			Measured %	Accumulated	True
550gCN	0.00098	0.07	9.7	1.1	8.6
TNP	0.00023	0.01	0.9	0.2	0.7
0.25gCN/TNP 2 h	0.00210	0.09	18.4	1.4	17.0
0.50gCN/TNP 2 h	0.00378	0.04	34.3	0.6	33.7
0.75gCN/TNP 2 h	0.00268	0.07	24.1	1.0	23.1

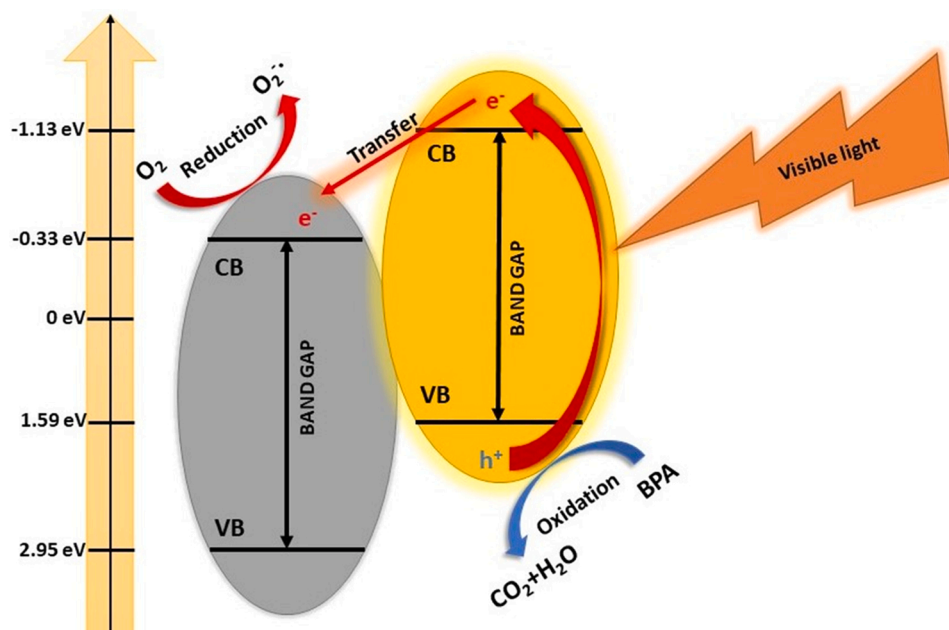


Fig. 13. Proposed photocatalytic mechanism based on the results of UV-Vis-DR and solid PL measurements. The yellow circle represents the g-C₃N₄ component and silver circle represents TiO₂. Under visible-light illumination, only g-C₃N₄ generates charge carriers, and the photogenerated electrons are injected into the conduction band (CB) of TiO₂. There, they reduce water-dissolved oxygen to form superoxide anionic radical (O₂^{•-}). The photo-generated holes remain in the valence band (VB) of g-C₃N₄, where they can directly oxidize water-dissolved and surface adsorbed bisphenol A (BPA). Both species are presented as the main species involved in the photodegradation of BPA under visible-light illumination.

electrons from CB of 550gCN to be injected into the CB of TNP. Annealing for 2 h at 350 °C increased the interface area between both components due to the relative thermal (in)stability of g-C₃N₄, which then enabled better injection of photogenerated electrons, thus reducing the charge carrier recombination rate. Further, from the estimated potential edges of CB and VB for both components, using the UV-Vis-DR and PL measurements, we suggested a charge carrier excitation and migration mechanism. The latter involves the photogenerated holes and superoxide anionic radicals as the purposed active species that can form hydroxyl radicals as seen in the results of experiments where coumarin was used as the OH-radical scavenger. The obtained results show that the visible-light triggered photocatalytic activity of pure g-C₃N₄ can be improved by an appropriate synthesis procedure and further enhanced by combining it with an adequate amount of TiO₂.

Funding sources

This work was supported by the Slovenian Research Agency (research core funding no. P2-0150 and P1-0417). The Slovenian Research Agency did not design, collect, analyze or interpret any data and was not involved in the submitting decision of the authors.

CRediT authorship contribution statement

Matevž Roškarič: Conceptualization, Investigation, Writing – original draft. **Gregor Žerjav:** Conceptualization, Investigation, Writing – original draft, Writing – review & editing, Supervision, Project administration. **Janez Zavašnik:** Investigation, Writing – review & editing. **Albin Pintar:** Resources. Writing – original draft, Writing – review & editing, Supervision, Project administration, Funding acquisition.

Declaration of Competing Interest

The authors declare that they have no known competing financial interests or personal relationships that could have appeared to influence the work reported in this paper.

Acknowledgements

The authors acknowledge the financial support from the Slovenian Research Agency for the young researcher grant. Acknowledgments also

go the CristalACTiV™ company for their generous donation of commercially available TiO₂ powder. Anja Sedminek is kindly acknowledged for her assistance in catalyst synthesis and catalyst activity screening.

Appendix A. Supporting information

Supplementary data associated with this article can be found in the online version at [doi:10.1016/j.jece.2022.107656](https://doi.org/10.1016/j.jece.2022.107656).

References

- [1] V. Vaiano, O. Sacco, D. Sannino, Electric energy saving in photocatalytic removal of crystal violet dye through the simultaneous use of long-persistent blue phosphors, nitrogen-doped TiO₂ and UV-light emitting diodes, *J. Clean. Prod.* 210 (2019) 1015–1021, <https://doi.org/10.1016/j.jclepro.2018.11.017>.
- [2] X. Yang, J.P.A. Wärna, J. Wang, P. Zhang, W. Luo, R. Ahuja, Enhanced overall water splitting under visible light of MoS₂/WSe₂ heterojunction by lateral interfacial engineering, *J. Catal.* 404 (2021) 18–31, <https://doi.org/10.1016/j.jcat.2021.09.004>.
- [3] M. Ismael, A review on graphitic carbon nitride (g-C₃N₄) based nanocomposites: synthesis, categories, and their application in photocatalysis, *J. Alloy. Compd.* 846 (2020), 156446, <https://doi.org/10.1016/j.jallcom.2020.156446>.
- [4] X. Ye, T. Zhu, Z. Hui, X. Wang, J. Wei, S. Chen, Revealing the transfer mechanisms of photogenerated charge carriers over g-C₃N₄/ZnIn₂S₄ composite: a model study for photocatalytic oxidation of aromatic alcohols with visible light, *J. Catal.* 404 (2021) 149–159, <https://doi.org/10.1016/j.jcat.2021.07.025>.
- [5] R. Andreozzi, V. Caprio, A. Insola, R. Marotta, Advanced oxidation processes (AOP) for water purification and recovery, *Catal* 53 (1999) 51–59, [https://doi.org/10.1016/S0920-5861\(99\)00102-9](https://doi.org/10.1016/S0920-5861(99)00102-9).
- [6] X. Li, S. Lyu, X. Lang, Superoxide generated by blue light photocatalysis of g-C₃N₄/TiO₂ for selective conversion of amines, *Environ. Res.* 195 (2021), 110851, <https://doi.org/10.1016/j.envres.2021.110851>.
- [7] R. Kaplan, B. Erjavec, A. Pintar, Enhanced photocatalytic activity of single-phase, nanocomposite and physically mixed TiO₂ polymorphs, *Appl. Catal. A-Gen.* 489 (2015) 51–60, <https://doi.org/10.1016/j.apcata.2014.10.018>.
- [8] G. Žerjav, J. Zavašnik, J. Kovač, A. Pintar, The influence of Schottky barrier height onto visible-light triggered photocatalytic activity of TiO₂ + Au composites, *Appl. Surf. Sci.* 543 (2021), 148799, <https://doi.org/10.1016/j.apsusc.2020.148799>.
- [9] N.F.F. Moreira, M.J. Sampaio, A.R. Riberio, C.G. Silva, J.L. Faria, A.M.T. Silva, Metal-free g-C₃N₄ photocatalysis of organic micropollutants in urban wastewater under visible light, *Appl. Catal. B* 248 (2019) 184–192, <https://doi.org/10.1016/j.apcatb.2019.02.001>.
- [10] G. Žerjav, A. Pintar, Influence of TiO₂ morphology and crystallinity on visible-light photocatalytic activity of TiO₂-Bi₂O₃ composite in AOPs, *Catalysts* 10 (2020) 395, <https://doi.org/10.3390/catal10040395>.
- [11] G. Žerjav, G. Scandura, C. Garlisi, G. Palmisano, A. Pintar, Sputtered vs. sol-gel TiO₂-doped films: characterization and assessment of aqueous bisphenol A oxidation under UV and visible light radiation, *Catal* 357 (2020) 380–391, <https://doi.org/10.1016/j.cattod.2019.09.027>.

- [12] G. Žerjav, M. Roškarič, J. Zavašnik, J. Kovač, A. Pintar, Effect of Au loading on Schottky barrier height in TiO₂ + Au plasmonic photocatalysts, *Appl. Surf. Sci.* 579 (2022), 152196, <https://doi.org/10.1016/j.apsusc.2021.152196>.
- [13] M. Sharma, S. Vaidya, A.K. Ganguli, Enhanced photocatalytic activity of g-C₃N₄-TiO₂ nanocomposites for degradation of Rhodamine B dye, *J. Photochem. Photobiol. A* 335 (2017) 287–293, <https://doi.org/10.1016/j.jphotochem.2016.12.002>.
- [14] B. Wu, L. Zhang, B. Jiang, Q. Li, C. Tian, Y. Xie, W. Li, H. Fu, Ultrathin porous carbon nitride bundles with an adjustable energy band structure toward simultaneous solar photocatalytic water splitting and selective phenylcarbinol oxidation, *Angew. Chem. Int. Ed.* 60 (2021) 4815–4822, <https://doi.org/10.1002/anie.202013753>.
- [15] H. Yu, R. Shi, Y. Zhao, T. Bian, Y. Zhao, C. Zhou, G.I.N. Waterhouse, L.-Z. Wu, C.-H. Tung, T. Zhang, Alkali-assisted synthesis of nitrogen deficient graphitic carbon nitride with tunable band structures for efficient visible-light-driven hydrogen evolution, *Adv. Mater.* 29 (2017), 1605148, <https://doi.org/10.1002/adma.201605148>.
- [16] J. Wang, S. Cao, J. Yu, Nanocages of polymeric carbon nitride from low-temperature supramolecular preorganization for photocatalytic CO₂ reduction, *Sol. RRL* 4 (2020), 1900469, <https://doi.org/10.1002/solr.201900469>.
- [17] R. Hao, G. Wang, H. Tang, L. Sun, C. Xu, D. Han, Template-free preparation of macro/mesoporous g-C₃N₄/TiO₂ heterojunction photocatalysts with enhanced visible light photocatalytic activity, *Appl. Catal. B* 187 (2016) 47–58, <https://doi.org/10.1016/j.apcatb.2016.01.026>.
- [18] C. Huang, Y. Wen, J. Ma, D. Dong, Y. Shen, S. Liu, H. Ma, Y. Zhang, Unraveling fundamental active units in carbon nitride for photocatalytic oxidation reactions, *Nat. Commun.* 12 (2021) 320, <https://doi.org/10.1038/s41467-020-20521-5>.
- [19] J. Wang, S. Yin, Q. Zhang, F. Cao, Y. Xing, Q. Zhao, Y. Wang, W. Xu, W. Wu, M. Wu, Single-Atom Fe-N₄ sites promote the triplet-energy transfer process of g-C₃N₄ for the photooxidation, *J. Catal.* 404 (2021) 89–95, <https://doi.org/10.1016/j.jcat.2021.09.010>.
- [20] L. Ma, G. Wang, C. Jiang, H. Bao, Q. Xu, Synthesis of core-shell TiO₂@g-C₃N₄ hollow microspheres for efficient photocatalytic degradation of rhodamine B under visible light, *Appl. Surf. Sci.* 430 (2018) 263–272, <https://doi.org/10.1016/j.apsusc.2017.07.282>.
- [21] K. Kočí, M. Reli, I. Troppová, M. Šihor, J. Kupková, P. Kustrowski, P. Praus, Photocatalytic decomposition of N₂O over TiO₂/g-C₃N₄ photocatalysts heterojunction, *Appl. Surf. Sci.* 396 (2017) 1685–1695, <https://doi.org/10.1016/j.apsusc.2016.11.242>.
- [22] H. Yan, Z. Zhu, Y. Long, W. Li, Single-source-precursor-assisted synthesis of porous WO₃/g-C₃N₄ with enhanced photocatalytic property, *Colloids Surf. A Physicochem. Eng. Asp.* 582 (2019), 123857, <https://doi.org/10.1016/j.colsurfa.2019.123857>.
- [23] Y. Yan, M. Yang, C. Wang, E. Liu, X. Hu, J. Fan, Defected ZnS/bulk g-C₃N₄ heterojunction with enhanced photocatalytic activity for dyes oxidation and Cr (VI) reduction, *Colloids Surf. A Physicochem. Eng. Asp.* 582 (2019), 123861, <https://doi.org/10.1016/j.colsurfa.2019.123861>.
- [24] Z. Mo, X. She, Y. Li, L. Liu, L. Huang, Z. Chen, Q. Zhang, H. Xu, H. Li, Synthesis of g-C₃N₄ at different temperatures for superior visible/UV photocatalytic performance and photoelectrochemical sensing of MB solution, *RSC Adv.* 5 (2015) 101552–101562, <https://doi.org/10.1039/C5RA19586A>.
- [25] PerkinElmer Technical note Infrared Spectroscopy, The Effects of Varying Force and Contact on ATR Spectra. (https://www.perkinelmer.com/cmsresources/im ages/44-135840tch_010127_01_atr.pdf), 2012 (Accessed 28 March 2022).
- [26] T. Durak, J. Depciuch, Effect of plant sample preparation and measuring methods on ATR-FTIR spectra results, *Environ. Exp. Bot.* 169 (2020), 103915, <https://doi.org/10.1016/j.envexpbot.2019.103915>.
- [27] W.-K. Jo, T.S. Natarajan, Influence of TiO₂ morphology on the photocatalytic efficiency of direct Z-scheme g-C₃N₄/TiO₂ photocatalysts for isoniazid degradation, *Chem. Eng. Sci.* 281 (2015) 549–565, <https://doi.org/10.1016/j.ces.2015.06.120>.
- [28] TM Chemistry LibreTexts, X-ray diffraction (XRD) basics and application. ([https://chem.libretexts.org/Courses/Franklin_and_Marshall_College/Introduction_to_Materials_Characterization_CHM_412/Collaborative_Text/Diffraction_Techniques/X-ray_diffraction_\(XRD\)_basics_and_application#title](https://chem.libretexts.org/Courses/Franklin_and_Marshall_College/Introduction_to_Materials_Characterization_CHM_412/Collaborative_Text/Diffraction_Techniques/X-ray_diffraction_(XRD)_basics_and_application#title)), 2020 (Accessed 28 March 2022).
- [29] B. Zhu, P. Xia, W. Ho, J. Yu, Isoelectric point and adsorption activity of porous g-C₃N₄, *Appl. Surf. Sci.* 344 (2015) 188–195, <https://doi.org/10.1016/j.apsusc.2015.03.086>.
- [30] J. Yang, X. Zhang, C. Xie, J. Long, Y. Wang, L. Wei, X. Yang, Preparation of g-C₃N₄ with high specific surface area and photocatalytic stability, *J. Electron. Mater.* 50 (2021) 1067–1074, <https://doi.org/10.1007/s11664-020-08654-1>.
- [31] Q. Lin, L. Li, S. Liang, M. Liu, J. Bi, L. Wu, Efficient synthesis of monolayer carbon nitride 2D nanosheet with tunable concentration and enhanced visible-light photocatalytic activities, *Appl. Catal. B* 163 (2015) 135–142, <https://doi.org/10.1016/j.apcatb.2014.07.053>.
- [32] Y.-H. Kim, C. Wolf, H. Kim, T.-W. Lee, Charge carrier recombination and ion migration in metal-halide perovskite nanoparticle films for efficient light-emitting diodes, *Nano Energy* 52 (2018) 329–335, <https://doi.org/10.1016/j.nanoen.2018.07.030>.
- [33] D. Das, S.L. Shinde, K.K. Nanda, Temperature-dependent photoluminescence of g-C₃N₄: implication for temperature sensing, *ACS Appl. Mater. Interfaces* 8 (2016) 2181–2186, <https://doi.org/10.1021/acsami.5b10770>.
- [34] G. Žerjav, A. Albreht, I. Vovk, A. Pintar, Revisiting terephthalic acid and coumarin as probes for photoluminescent determination of hydroxyl radical formation rate in heterogeneous photocatalysis, *Appl. Catal. A-Gen.* 598 (2020), 117566, <https://doi.org/10.1016/j.apcata.2020.117566>.
- [35] H. Zhang, F. Liu, H. Wu, X. Cao, J. Sun, W. Lei, *In situ* synthesis of g-C₃N₄/TiO₂ heterostructures with enhanced photocatalytic hydrogen evolution under visible light, *RSC Adv.* 7 (2017) 40327–40333, <https://doi.org/10.1039/C7RA06786K>.
- [36] S. Zhao, S. Chen, H. Yu, X. Quan, g-C₃N₄/TiO₂ hybrid photocatalyst with wide absorption wavelength range and effective photogenerated charge separation, *Sep. Purif. Technol.* 99 (2012) 50–54, <https://doi.org/10.1016/j.seppur.2012.08.024>.
- [37] S. Albert-Seifried, D.-H. Ko, S. Hüttner, C. Kanimozhi, S. Patil, R.H. Friend, Efficiency limitations in a low band-gap diketopyrrolopyrrole-based polymer solar cell, *Phys. Chem. Chem. Phys.* 16 (2014) 6743–6752, <https://doi.org/10.1039/C4CP00485J>.
- [38] H. Li, L. Zhou, L. Wang, Y. Liu, J. Lei, J. Zhang, *In situ* growth of TiO₂ nanocrystals on g-C₃N₄ for enhanced photocatalytic performance, *Phys. Chem. Chem. Phys.* 17 (2015) 17406–17412, <https://doi.org/10.1039/C5CP02554K>.
- [39] P. Lin, H. Hu, H. Lv, Z. Ding, L. Xu, D. Qian, P. Wang, J. Pan, C. Li, C. Cui, Hybrid reduced graphene oxide/TiO₂/graphitic carbon nitride composites with improved photocatalytic activity for organic pollutant degradation, *Appl. Phys. A* 124 (2018) 510, <https://doi.org/10.1007/s00339-018-1933-6>.
- [40] C. Hu, W.-Z. Hung, M.-S. Wang, P.-J. Lu, Phosphorus and sulfur codoped g-C₃N₄ as an efficient metal-free photocatalyst, *Carbon* 127 (2018) 374–383, <https://doi.org/10.1016/j.carbon.2017.11.019>.
- [41] A. Houas, H. Lachheb, M. Ksibi, E. Elaloui, C. Guillard, J.-M. Herrmann, Photocatalytic degradation pathway of methylene blue in water, *Appl. Catal. B* 31 (2001) 145–157, [https://doi.org/10.1016/S0926-3373\(00\)00276-9](https://doi.org/10.1016/S0926-3373(00)00276-9).
- [42] M. Fu, J. Liao, F. Dong, H. Li, H. Liu, Growth of g-C₃N₄ layer on commercial TiO₂ for enhanced visible light photocatalytic activity, *J. Nanomater.* 2014 (2014), <https://doi.org/10.1155/2014/869094>.
- [43] A.H. Jawad, N.S.A. Mubarak, M.A.M. Ishak, K. Ismail, W.I. Nawawi, Kinetics of photocatalytic decolorization of cationic dye using porous TiO₂ film, *J. Taibah Univ. Sci.* 10 (2016) 352–362, <https://doi.org/10.1016/j.jtusci.2015.03.007>.
- [44] B. Liu, M. Qiao, Y. Wang, L. Wang, Y. Gong, T. Guo, X. Zhao, Persulfate enhanced photocatalytic degradation of bisphenol A by g-C₃N₄ nanosheets under visible light irradiation, *Chemosphere* 189 (2017) 115–122, <https://doi.org/10.1016/j.chemosphere.2017.08.169>.
- [45] Y. Yang, Y. Guo, F. Liu, X. Yuan, Y. Guo, S. Zhang, W. Guo, M. Huo, Preparation and enhanced visible-light photocatalytic activity of silver deposited graphitic carbon nitride plasmonic photocatalyst, *Appl. Catal. B* 142–143 (2013) 828–837, <https://doi.org/10.1016/j.apcatb.2013.06.026>.
- [46] S. Cao, J. Yu, g-C₃N₄-based photocatalysts for hydrogen generation, *J. Phys. Chem. Lett.* 5 (2014) 2101–2107, <https://doi.org/10.1021/jz500546b>.
- [47] B. Chai, T. Peng, J. Mao, K. Li, L. Zan, Graphitic carbon nitride (g-C₃N₄)-Pt-TiO₂ nanocomposite as an efficient photocatalyst for hydrogen production under visible light irradiation, *Phys. Chem. Chem. Phys.* 14 (2012) 16745–16752, <https://doi.org/10.1039/C2CP42484C>.
- [48] Y. He, L. Zhang, B. Teng, M. Fan, New application of Z-scheme Ag₃PO₄/g-C₃N₄ composite in converting CO₂ to Fuel, *Environ. Sci. Technol.* 49 (2015) 649–656, <https://doi.org/10.1021/es5046309>.
- [49] L. Zhang, J. Zhang, H. Yu, J. Yu, Emerging S-scheme photocatalyst, *Adv. Mater.* 34 (2022), 2107668, <https://doi.org/10.1002/adma.202107668>.